PlanetProfile: Self-consistent interior structure modeling for terrestrial bodies in Python

M. J. Styczinski[1,2], S. D. Vance[2], and M. Melwani Daswani[2]

[1]NASA Postdoctoral Program Fellow, Jet Propulsion Laboratory, California Institute of Technology, Pasadena, California, USA

[2]Jet Propulsion Laboratory, California Institute of Technology, Pasadena, California, USA

Key Points:

- Radial models of planetary interiors are generated from bulk properties based on geophysical models, lab data, and minimal assumptions
- Bodies with a high moment of inertia such as Callisto require low-density rocks, which we model with a high effective porosity
- Cross-comparison of magnetic induction and gravity analysis demonstrates a narrowed parameter space for the properties of Europa's ocean

Corresponding author: Marshall Styczinski, `marshall.j.styczinski@jpl.nasa.gov`

Abstract

The open-source *PlanetProfile* framework was developed to investigate the interior structure of icy moons based on self-consistency and comparative planetology. The software, originally written in Matlab, relates observed and measured properties, assumptions such as the type of materials present, and laboratory equation-of-state data through geophysical and thermodynamic models to evaluate radial profiles of mechanical, thermodynamic, and electrical properties, as self-consistently as possible. We have created a Python version of *PlanetProfile*. In the process, we have made optimization improvements and added parallelization and parameter-space search features to utilize fast operation for investigating unresolved questions in planetary geophysics, in which many model inputs are poorly constrained. The Python version links to other scientific software packages, including for evaluating equation-of-state data, magnetic induction calculations, and seismic calculations. Physical models in *PlanetProfile* have been reconfigured to improve self-consistency and generate the most realistic relationships between properties. Here, we describe the software design and algorithms in detail, summarize models for major moons across the outer solar system, and discuss new inferences about the interior structure of several bodies. The high values and narrow uncertainty ranges reported for the axial moments of inertia for Callisto, Titan, and Io are difficult to reconcile with self-consistent models, requiring highly porous rock layers equivalent to incomplete differentiation for Callisto and Titan, and a high rock melt fraction for Io. This effect is even more pronounced with the more realistic models in the Python version. Radial profiles for each model and comparison to prior work are provided as Zenodo archives.

Plain Language Summary

The software package *PlanetProfile* was developed in order to connect measurable properties of planetary bodies to each other and determine how planetary interiors might be structured. We adapted the existing Matlab version of *PlanetProfile* to Python and improved it in many ways in the process, to better investigate scientific questions. Python is more widely available, and *PlanetProfile* now connects better to other scientific software packages capable of relating measurements and observations to the interior structure of planetary bodies such as large moons. *PlanetProfile* is now more adaptable for new scientific investigations and for adding features, includes more realistic relationships between pressures, temperatures, and physical properties of materials, and is optimized

for studies that require a wide variety of models to be run. These improvements make *PlanetProfile* a powerful tool that will become more useful as new features are added. We summarize our models for the major large moons in the outer solar system and provide output files detailing each model. In creating these models, we found that bulk properties for Io, Callisto, and Titan are difficult to include self-consistently, which suggests that the reported values may contain errors.

1 Introduction

Liquid water oceans are common among the large moons of the outer planets (Nimmo & Pappalardo, 2016). Evidence supporting present-day subsurface oceans comes from a wide variety of sources, including measurements of magnetic fields (Kivelson et al., 2000), gravity fields (Nimmo et al., 2016), geodesy (Beuthe et al., 2016), libration (Thomas et al., 2016), and more. Water is a requirement for all known life on Earth (Cockell et al., 2016; Westall & Brack, 2018), so finding it in great abundance is an exciting development in the search for life elsewhere. Understanding the physical and chemical conditions present in these oceans is therefore critical to understanding whether they may be habitable (Vance et al., 2018) and what types of organisms may be found there (Rothschild & Mancinelli, 2001).

The long tradition of geophysical investigation of Earth has demonstrated the importance of synthesizing information from a variety of observational and theoretical methods for understanding the properties of material layers at inaccessible depths (*e.g.,* Dziewonski & Anderson, 1981). Constraining the conditions of interior layers of icy moons requires a similar synthesis. Compared to studies at Earth, measurements from the outer solar system will always be sparse, thus forcing a greater emphasis on global-scale modeling efforts.

There are myriad ways to combine the available information into models of layered interior structure. Although planetary bodies are always inherently 3D in their structure, it is instructive to approximate the bodies as spherically symmetric, as this will generally be true to first order for most physical properties. Lateral variations can then be added as perturbations to the symmetric, radial model. The open-source software framework *PlanetProfile* has emerged from such efforts to model the interior structure of icy

Available on GitHub at `https://github.com/NASA-Planetary-Science/PlanetProfile`.

moons (Vance et al., 2014, 2016). The guiding principle upon which *PlanetProfile* is built is self-consistency: a harmonious relationship between all model inputs, assumptions, and outputs, such that there is no internal inconsistency. Many physical properties of planetary bodies, especially in the outer solar system, are unknown and must be assumed. However, among the properties that are measured or rigorously inferred, self-consistent modeling provides a crucial link needed to derive bounding constraints that satisfy known conditions and span the breadth of reasonable assumptions. Self-consistent models thus represent a robust method for combining measurements from multiple investigations into coherent first-order constraints on interior structure.

PlanetProfile was originally written in Matlab and focused on Europa, Ganymede, Callisto, Enceladus, and Titan (Vance et al., 2018). The software combines bulk properties such as mass, axial moment of inertia, and surface radius, along with surface properties such as mean temperature and pressure, with several assumed properties to calculate depth profiles of geophysically important quantities, such as temperature, pressure, density, seismic wave velocities, electrical conductivity using geophysical models, thermodynamic models, and laboratory equation-of-state (EOS) measurements. We have converted the entirety of the software to Python, with the intent to improve accessibility and organization of the framework. The Supplemental Information includes a comparison of Python *PlanetProfile* outputs for the models analogous to those studied by Vance et al. (2018). These comparison models are also provided as a Zenodo archive: `https://doi.org/10.5281/zenodo.7318029`.

We have generalized the approach of *PlanetProfile* to be applicable to waterless bodies (*e.g.,* Io) and constructed models for major moons spanning the outer solar system and Pluto based on constraints available in the literature. In the process of converting the software to Python, we have made many improvements to the self-consistent modeling approach, optimization of the computational architecture, and integration with related software packages available in Python. The primary purpose of this work is to describe the improved self-consistent modeling approach and the features we have implemented to enable applicability to many solar system bodies (Section 2). We also present model results for bodies across the outer solar system (Section 3: Figures 5 – 9 and Tables 5 – 9) and discuss new insights obtained using the updated solution method in Section 4. In particular, Io, Callisto, and Titan are challenging to model self-consistently, owing to likely solid-state mantle convection and/or incomplete differentiation. High rock

porosities are required in these models to match spacecraft observations of their bulk properties and gravity field, simulating a lack of differentiation or partial melt (see Section 4).

1.1 Note About Matching and Uncertainty of the Axial Moment of Inertia

Degree-2 coefficients in the gravitational potential of a body (*e.g.,* J_2 and C_{22}) relate to the configuration of mass within the body, and therefore can be used to probe the interior structure. These coefficients can be measured via the Doppler shift in radio signals exchanged with spacecraft during flybys of the body (Anderson et al., 1998). It is typical to then assume that the body is in hydrostatic equilibrium—*i.e.,* the layers do not support stresses capable of maintaining a shape departing from the lowest-gravitational-energy configuration, as in a fluid with no rigidity. In the hydrostatic case, the Radau–Darwin approximation (Rambaux & Castillo-Rogez, 2013) can be applied to determine the axial moment of inertia C, often reported in dimensionless units as C/MR^2 (and simply called the moment of inertia, MoI). This quantity is useful as a metric to constrain the interior structure of planetary bodies, as it can be calculated from depth profiles of mass density and compared to the measured value. For a spherical body of uniform mass density, $C/MR^2 = 2/5$. The lower the measured value of C/MR^2, the more concentrated is the mass inside the body. In this way, measurements of the gravitational field of numerous moons (*e.g.,* Anderson, Jacobson, Lau, et al., 2001; Anderson et al., 1998, 1996; Anderson, Jacobson, McElrath, et al., 2001) have been used to infer the MoI for these bodies. However, departure from hydrostatic conditions is likely (*e.g.,* McKinnon, 2006; Gao & Stevenson, 2013). Applying the Radau–Darwin approximation in these cases will result in a true MoI less than the reported value by as much as a few percent (Gao & Stevenson, 2013). Gao and Stevenson (2013) consider a 3% variation as within the uncertainty in gravitational coefficients of Callisto and other moons, though they also note that the hydrostatic assumption can result in MoI values as much as 10% away from the true value. To account for such variation, in *PlanetProfile* the upper and lower bounds for MoI matching can be independently set to a wider range than the tight 1σ uncertainties quoted in the literature.

Table 1. Data sources for equation-of-state (EOS) measurements and the range over which the measurements can be interpolated in pressure P, temperature T, and salinity w. Units for salinity are in g solute per kg total solution. The spline fits used to interpolate tabular data can be used to extrapolate to a greater range of P, T, and w conditions in most cases. No spline fit is used for Seawater EOS data; Seawater ocean models are therefore limited to bodies the size of Europa (radius 1560 km) and smaller.

Material	EOS evaluation	P valid (MPa)	T valid (K)	w valid ($\mathrm{g\,kg^{-1}}$)
Ice (Ih, II, III, V, VI)	*SeaFreeze*[abc]	$0 - 2300$	$73 - 500$	-
CH_4 clathrate (phase stability)	Fit to data from literature[d]	$0.1 - 20$	$200 - 290$	-
CH_4 clathrate (density and seismic)	Parameterization from literature[e]	$30 - 98$	$253 - 288$	-
CH_4 clathrate (thermodynamic)	Parameterization from literature[f]	$0.1 - 100$	$5 - 292$	-
Liquid water (pure)	*SeaFreeze*[g]	$0.1 - 2300$	$240 - 500$	-
$MgSO_4$(aq)	Parameterization and data from literature[hij]	$0.1 - 800$	$253 - 373$	$0 - 231$
Seawater	*Gibbs Seawater (TEOS-10)*[k]	$0.1 - 100$	$250 - 373$	$0 - 50$
Rocky layers ("silicates")	*Perple_X*[l]	$0.1 - 14000$	$273 - 2000$	-
Iron + sulfur (metallic) core	*Perple_X*[l]	$0.1 - 14000$	$273 - 2000$	-

[a] Available on GitHub (and PyPI): `https://github.com/Bjournaux/SeaFreeze`

[b] Feistel and Wagner (2006) (Ih)

[c] Journaux et al. (2020) (II, III, V, VI)

[d] Choukroun et al. (2010)

[e] Helgerud et al. (2009)

[f] Ning et al. (2015)

[g] Bollengier et al. (2019)

[h] Vance et al. (2014) (phase transitions)

[i] Vance and Brown (2013) (physical properties)

[j] Vance et al. (2018) (electrical properties)

[k] McDougall and Barker (2011), `https://www.teos-10.org/software.htm`

[l] Connolly (2009), `https://www.perplex.ethz.ch/`. *Perple_X* uses mineral data from multiple sources—see Table 2.

Table 2. Sources of EOS data from the literature used for minerals implemented by *Perple_X*.

Model name	Mineral type	Data source
Atg(PN)	Antigorite	Padrón-Navarta et al. (2013)
Bi(HGP)	Biotite	(Holland et al., 2018)
Chl(HP)	Chlorite	(Holland et al., 1998)
COH-Fluid	$CO_2-CH_4-H_2-CO-H_2O-H_2S-SO_2-N_2-NH_3$ fluid with linear subdivisions	(Connolly & Galvez, 2018)
Cpx(HGP)	Clinopyroxene	(Holland et al., 2018)
Do(HP)	Dolomite-ankerite	(Holland & Powell, 1998)
Gt(HGP)	Garnet	(Holland et al., 2018)
M(HP)	Magnesite-siderite-rhodochrosite	(Holland & Powell, 1998)
melt(HGP)	Generic silicate melt	(Holland et al., 2018)
Mica(CF)	Fe−Mg−K−Na mica	(Chatterjee & Froese, 1975; Holland & Powell, 1998)
O(HGP)	Olivine	(Holland et al., 2018)
Omph(GHP)	Omphacite	(Green et al., 2007)
Opx(HGP)	Orthopyroxene	(Holland et al., 2018)
Pl(JH)	Plagioclase	(Jennings et al., 2016)
Pu	Pumpellyite	(Holland & Powell, 2011)[a]
Sp(HGP)	Spinel	(Holland et al., 2018)
Stlp	Stilpnomelane	(Holland & Powell, 2011)[a]
T	Talc	(Holland & Powell, 2011)[a]

[a] Implemented with the `DEW17HP622ver_elements` *Perple_X* data file—see `https://www.perplex.ethz.ch/perplex_thermodynamic_data_file.html`.

2 Self-Consistent Model Design

PlanetProfile is designed around self-consistency. This principle is achieved and maintained by making as few assumptions as possible while still enabling a determination of the physical properties as a function of depth that result from measured and assumed inputs. Physical properties are determined for each material from interpolation of laboratory measurements of these properties over many different temperatures and pressures, known as equation-of-state (EOS) measurements. Table 1 lists the software sources of EOS evaluation available in *PlanetProfile* for each currently supported material type. The material type within each major layer (rocks, core, *etc.*) is assumed to be uniform, except in cases where porosity is modeled (Section 2.4). In *PlanetProfile*, "silicates" is used as a shorthand to refer to any rocky material, and includes a variety of minerals. The minerals modeled in *PlanetProfile* using *Perple_X* are listed along with the data sources in Table 2.

Table 3 lists the measured inputs required by *PlanetProfile*, along with values used for selected moons in this work. Measured inputs are used to match the bulk physical characteristics of the modeled body. Table 4 lists the assumed inputs required by *PlanetProfile* along with the range or set of values we have modeled. The assumed inputs are required in order to have enough information to solve for the unknown properties. Certain critical assumptions—namely the ocean solute composition, salinity, and melting temperature (if an ocean is present)—must be supposed from inferences based on laboratory measurements (*e.g.,* Zolotov & Kargel, 2009), surface reflectance spectra (*e.g.,* Trumbo et al., 2019), indirect sampling (*e.g.,* Glein & Waite, 2020), plausible building block composition (*e.g.,* Melwani Daswani et al., 2021), *etc.* Methane clathrate hydrate (sI) is optionally modeled as a conductive lid, an ice shell underplate, or throughout the ice shell, with stability determined from a parameterization to data from Choukroun et al. (2010).

To make the problem tractable, each material layer (ice, rock, *etc.*) is divided into a number of discrete layers. The number of layers sets the resolution of the output model and controls the total run time, typically 0.5−10 s. The primary output from *PlanetProfile* is an ASCII text file containing columns describing physical properties of each discrete layer as a function of depth (and radius). This output is referred to as a profile.

Table 3. Measured bulk properties required as inputs by *PlanetProfile*, along with values used in default models for varied example bodies. Several properties, such as surface radius, temperature, and pressure, are used directly as calculation starting points. Other properties, such as mass and axial moment of inertia (MoI), are used to determine profile validity and select a matching, self-consistent profile. A full list of the bulk properties for default models included in *PlanetProfile* is detailed in Tables 10 – 13.

Property	Io	Ganymede	Enceladus
Radius R (km)[a]	1821.49	2631.2	252.1
Total mass M (kg)	8.932×10^{22} [b]	1.4819×10^{23} [b]	1.08022×10^{20} [c]
Axial MoI C/MR^2 [d]	$0.37685^{+0.00035}_{-0.01166}$ [e]	$0.3115^{+0.0028}_{-0.0121}$ [f]	$0.335^{+0.001}_{-0.011}$ [g]
Surface pressure P_{surf} (MPa)	0	0	0
Surface temperature T_{surf} (K)	110	110	75

[a] Mean radii from Archinal et al. (2018)

[b] Hussmann et al. (2006)

[c] Jacobson et al. (2006)

[d] Lower values increased by 3% of mean value per Gao and Stevenson (2013)

[e] Anderson, Jacobson, Lau, et al. (2001)

[f] Schubert et al. (2004)

[g] Iess et al. (2014)

Table 4. Assumed properties required as inputs by *PlanetProfile* for calculation of self-consistent depth profiles. Default inputs are listed for the same example bodies as in Table 3. Ice bottom temperatures are each selected to be consistent with the range of ice shell thickness supported by published studies. Surface heat flux is calculated for icy bodies from the thermal conductivity of the ice shell conductive lid; this quantity is an input for waterless bodies. Rock compositions are consistent with a differentiated body, such that the total elemental inventory of rock + core matches the modeled chondritic material, assuming all free fluids (volatiles) are lost to the hydrosphere or escape from the body. A full list of bulk properties for the default models included in *PlanetProfile* are detailed in Tables 10 – 13.

Property	Io	Ganymede	Enceladus
Ocean composition and salinity w	N/A	Pure H_2O	$10\,\mathrm{g\,kg^{-1}}$ Seawater
Ice bottom temperature T_b	N/A	258.86 K	272.4578 K
Surface heat flux q_{surf}	$0.14\,\mathrm{W\,m^{-2}}$	N/A	N/A
Rock composition	CV chondrite	CM chondrite	Comet 67P/C–G
Core FeS/(Fe+FeS) ratio x_{FeS}	12.5 wt% FeS	20 wt% FeS	not modeled
Ice porosity in vacuum ϕ_{ice}	N/A	not modeled	not modeled
Ice pore closure pressure $P_{c,\mathrm{ice}}$	-	-	-
Rock porosity in vacuum ϕ_{rock}	70 vol%	not modeled	32 vol%
Rock pore closure pressure $P_{c,\mathrm{rock}}$	750 MPa	-	350 MPa

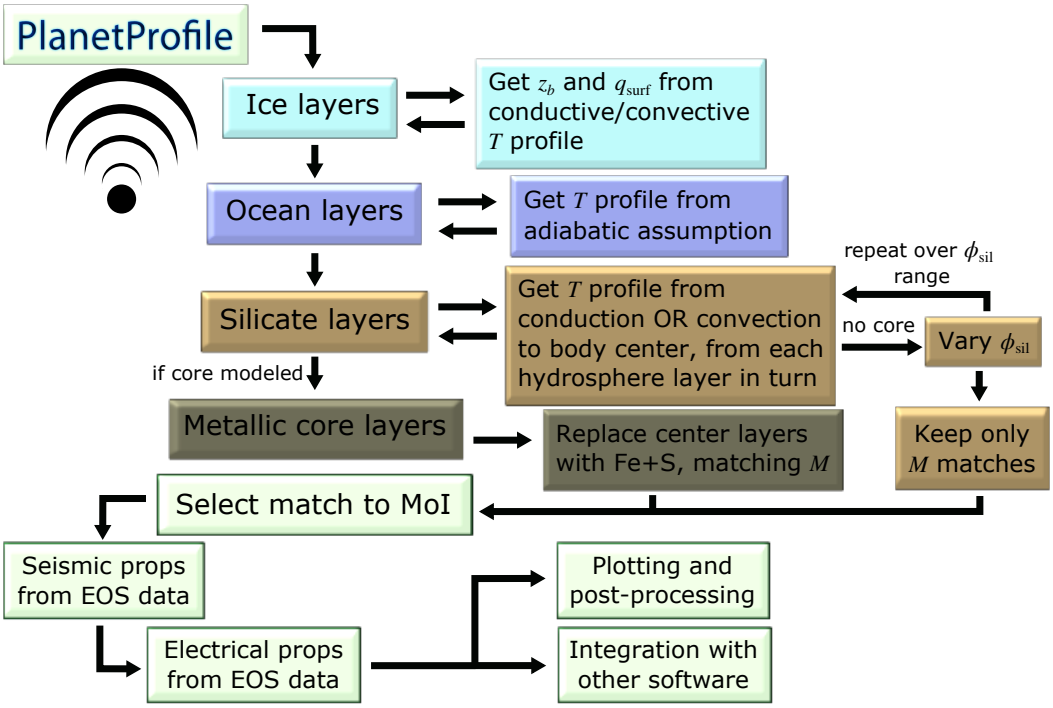

Figure 1. Overall design of *PlanetProfile* self-consistent models of interior structure. For waterless bodies, ice/ocean layers are skipped and q_{surf} is an input. z_b: ice shell thickness; q_{surf}: surface heat flux; T: layer temperature; ϕ_{rock}: rock porosity at 0 pressure; M: total body mass.

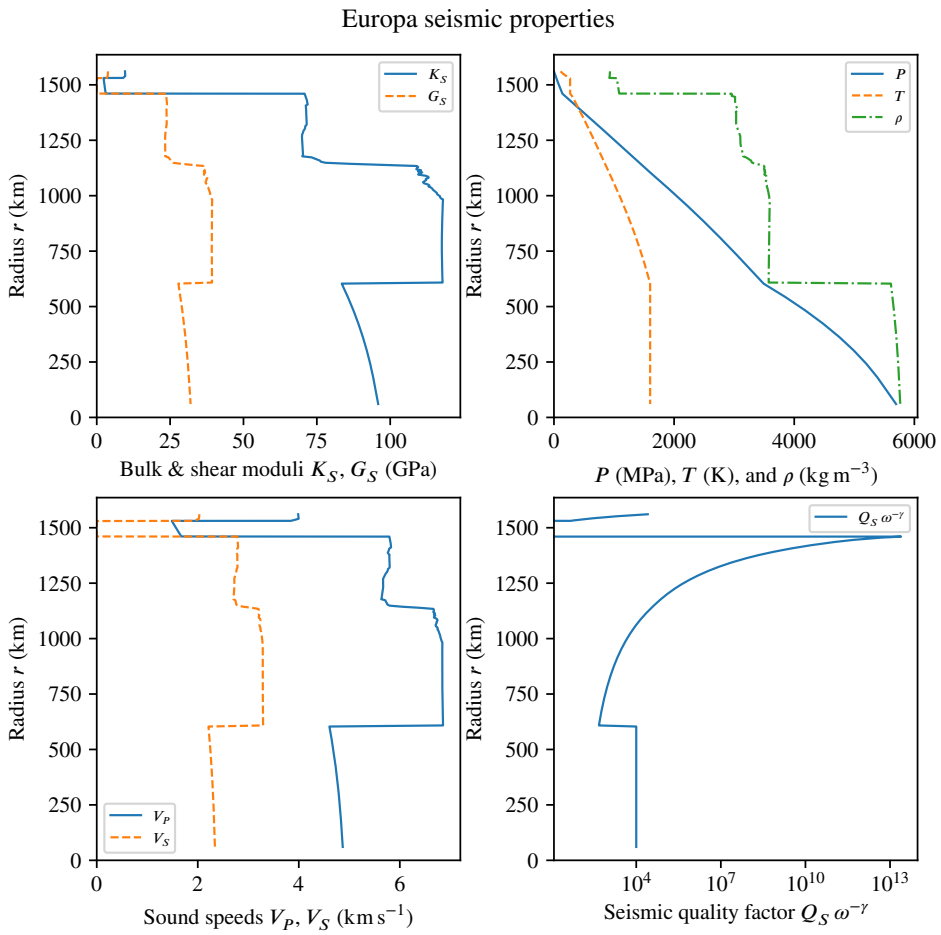

Figure 2. Example output figure from *PlanetProfile* containing seismic properties, including sound speeds V_P and V_S, pressure P, temperature T, density ρ, bulk and shear moduli K_S and G_S, and seismic quality factor $Q_S\,\omega^{-\gamma}$. The input model for Europa is the default listed in Table 10, with outputs detailed in Table 6 and Figure 6.

Figure 1 shows the basic organization of the self-consistent model calculations. Except for bodies like Io lacking surface water, the hydrosphere is calculated first. For the hydrosphere, the first step is to determine the pressure consistent with the assumed melting temperature, ocean composition, and salinity from laboratory EOS measurements. The properties of the ice shell are next calculated by first assuming a conductive thermal profile with no internal heating, then recalculated if convection is expected based on the Rayleigh number Ra. An adiabatic thermal profile is assumed within the ocean. Properties of rock and possible core layers are then calculated together, starting from each hydrosphere layer in turn and with core radius scaled to match the total body mass. When a core is not modeled, the rock properties are calculated for a range of porosities, retaining the mass-matching rock profile for each. Lastly, the overall profile with a calculated MoI nearest to the input MoI is selected, with seismic and electrical properties calculated for the full profile. If no calculated MoI lies within the uncertainty of the input MoI, the input configuration is deemed invalid. An example output showing several relevant properties for a profile of Europa is shown in Figure 2.

2.1 Ice Layers

The properties of surface ice layers are primarily set by the assumed bottom temperature T_b. At the surface is typically ice Ih, although methane clathrate may also be assumed to be present (Section 2.1.4). For thick ice shells on larger bodies like Ganymede, the pressures at the bottom of the surface ice Ih layer may be consistent with ice III (Section 2.1.3). Calculations are thus initiated by querying the ocean EOS (see Table 1) for the phase expected for the input T_b over a range of pressures above the surface pressure P_{surf}. The bottom pressure P_b consistent with the phase transition from ice Ih to another phase (liquid or ice III) is used to set the initial ice profile.

2.1.1 Initial Ice Shell Thermal Profile

To start, the ice shell properties are calculated from the ice Ih EOS implemented by *SeaFreeze* assuming a conductive thermal profile with the Fourier heat law (Turcotte & Schubert, 2002):

$$q = -k\frac{\partial T}{\partial r}, \tag{1}$$

where q is the upward heat flux passing through a spherical surface at radius r and k is the thermal conductivity at that surface. The thermal conductivity of ice layers is assumed to follow a $k \sim 1/T$ dependence (Andersson & Inaba, 2005). If we further assume q, local gravitational acceleration g, and layer mass density ρ are approximately constant throughout the ice shell, Equation 1 can be manipulated to obtain

$$T(P) = T_{\mathrm{bot}}^{\frac{P-P_{\mathrm{top}}}{P_{\mathrm{bot}}-P_{\mathrm{top}}}} T_{\mathrm{top}}^{\frac{P_{\mathrm{bot}}-P}{P_{\mathrm{bot}}-P_{\mathrm{top}}}}. \tag{2}$$

In Equation 2, subscript "bot" and "top" refer to pressures P and temperatures T at the bottom and top of the ice shell, respectively. Although use of this relation represents a departure from self-consistency, as we later determine ρ and g as a function of depth, the differences will be slight except in very thick shells, where convection is expected. In those cases, the thermal profile is reassigned to account for convection (Section 2.1.2), and the properties are recalculated from the ice EOS.

The material layer is next divided into a set number of layers n_{iceIh} with a linear step in pressure, from P_{surf} to P_b, and the temperatures are assigned as in Equation 2. The physical properties (mass density ρ, heat capacity at constant pressure C_P, thermal expansivity α) are then calculated from the ice EOS using *SeaFreeze*. Finally, the thickness $\Delta z = z_i - z_{i-1}$ of each (i^{th}) layer is calculated, propagating downward from the surface, with

$$z_i = z_{i-1} + \frac{P_i - P_{i-1}}{g_{i-1}\rho_{i-1}}, \tag{3}$$

$$g_{i-1} = \frac{G(M - m_{\mathrm{above}})}{r_i^2}, \tag{4}$$

where G is the gravitation constant, M is the total body mass, and m_{above} is the sum of layer masses above layer i as determined from each layer's radius and density, resulting in $z_b = z_{n_{\mathrm{iceIh}}}$. Equation 4 follows from Gauss's law and Equation 3 follows from the local approximation $\Delta P = \rho g \Delta z$.

2.1.2 Ice Shell Convection

Once the physical properties have been calculated from the conductive profile in the ice, the Rayleigh number Ra and critical Rayleigh number Ra_{crit} can be calculated to assess whether solid-state convection is expected. The parameterization for ice shell convection implemented in *PlanetProfile* is that of Deschamps and Sotin (2001). These authors defined scaling laws for the thermal profile of convecting ice layers based on 2D

thermodynamics simulations. When the calculated Rayleigh number is greater than the critical Rayleigh number, the thermal profile is reassigned according to the scaling laws from Deschamps and Sotin (2001), with a thin lower thermal boundary layer (TBL), nearly isothermal convecting region, and conductive lid. The relevant quantities are calculated from the following relations (after Deschamps & Sotin, 2001):

$$Ra = \frac{\alpha C_P \rho g (T_b - T_{\rm top}) z_b^3}{\eta_{\rm conv} k} \tag{5}$$

$$\eta(T) = \eta_{\rm melt} \exp\left\{ A \left(\frac{T_{\rm melt}}{T} - 1 \right) \right\}, \tag{6}$$

$$T_{\rm conv} = B \left(\sqrt{1 + \frac{2}{B}(T_b - C)} - 1 \right), \tag{7}$$

$$A = \frac{E_{\rm act}}{R T_b},\ B = \frac{E_{\rm act}}{2 R c_1},\ C = c_2 (T_b - T_{\rm top}),\ c_1 = 1.43,\ c_2 = -0.03,$$

with $T_{\rm conv}$ the temperature at the top of the convecting region, α the thermal expansivity, C_P the heat capacity at constant pressure, ρ the mass density, g the acceleration due to gravity, $\eta_{\rm conv} = \eta(T_{\rm conv})$ the viscosity at the convecting temperature, R the ideal gas constant, $E_{\rm act}$ the activation energy for diffusion, and c_1, c_2 are fit parameters from the results of Deschamps and Sotin (2001). All quantities are in SI units (temperatures in K) except $E_{\rm act}$, which is in J/mol, and R, which is in J/mol/K. The critical Rayleigh number $Ra_{\rm crit}$ is calculated using (Solomatov, 1995; Hammond et al., 2016)

$$Ra_{\rm crit} = 20.9 \left(\frac{E_{\rm act}(T_b - T_{\rm top})}{R T_{\rm conv}^2} \right)^4. \tag{8}$$

The Rayleigh number is defined for a region with uniform physical properties. In *PlanetProfile*, except where top or bottom values are specified, we evaluate physical properties at the midpoint in pressure ($(P_{\rm surf} + P_b)/2$) and at the convecting temperature after Solomatov (1995).

The method of Deschamps and Sotin (2001) prescribes layer thicknesses for the conductive lid and lower TBL based on the quantities in Equations 5 – 7. If the sum of these thicknesses exceeds the ice shell thickness z_b evaluated with the conductive profile, convection is assumed to be absent. Otherwise, a conductive profile is assigned to these upper and lower layers using Equation 2 and an adiabatic thermal profile is assigned to the convecting region using the procedure detailed for the ocean layers with Equation 9 (see Section 2.2).

Last, the heat flux through the ice shell is determined from the temperature difference across the lower TBL and the thermal conductivity in the convecting region us-

ing Equation 1. For shells where convection is not modeled or not occurring, the heat flux is determined using the temperature difference and thermal conductivity across the bottom ice layer. Tidal heating is not currently implemented in the ice shell, so this heat flux value is multiplied by the area of a sphere with radius $r = R - z_b$ to get the total rate of heat loss upward through the ice shell. This value is later scaled to the heat flux from the rock layers into the hydrosphere by dividing by the surface area of a sphere with the radius at that location (Section 2.3), and also to derive the heat flux at the surface q_{surf} using the surface radius R.

2.1.3 Ice III, V Underplate

For cold, thick ice shells, ice III and even ice V may be present between the surface ice Ih and liquid ocean. Ice V is stable at higher pressures (above 350 MPa) than ice III (above 209 MPa), so underplating ice V is assumed to only co-occur with ice III. Such underplate layers, in direct contact with the surface ice shell, must be toggled on manually and require additional input parameters $T_{b,\mathrm{III}}$ and $T_{b,\mathrm{V}}$ to be assumed. The assumed values of $T_{b,\mathrm{III}}$ and $T_{b,\mathrm{V}}$ must be consistent with the phase diagram for each material. The properties of ice III and V underplate layers are evaluated as with ice Ih, by first supposing an initial conductive profile from Equation 2, then checking for convection using the parameterization described in Section 2.1.2. A benefit of this parameterization is that the required inputs are sufficiently general as to apply to a wide range of viscous materials for which the activation energy can be measured or estimated.

2.1.4 Methane Clathrates

Methane clathrate hydrates (often simply called "clathrates") may play an important role in determining the properties of ice shells for several bodies (Mousis et al., 2015), especially Titan (Choukroun et al., 2010) and Pluto (Kamata et al., 2019), due to their high rigidity and low thermal conductivity compared to ice Ih, and their expected presence among high-volatile-content bodies. Their properties make them somewhat difficult to model self-consistently. To allow for modeling different possible configurations, three options are implemented in *PlanetProfile* for including clathrates in the ice shell: (1) conductive lid, (2) whole shell, (3) underplate. In each case, where clathrates are present they are assumed to replace ice Ih for the purpose of determining layer properties. Stability of clathrates is assessed by a common dissociation curve, based on the data pre-

sented by Choukroun et al. (2010), originally from Sloan (1998). For calculations, clathrates are divided into a number of discrete layers n_{clath}.

In the conductive lid model, clathrates are assumed to occupy an initial maximum thickness at the surface, which can be reduced if the dissociation temperature is exceeded along the conductive profile. After the conductive profile is evaluated, the Rayleigh number and critical Rayleigh number are calculated as with an ice Ih shell. If convection is expected, the clathrate phase is restricted to the conductive lid portion, such that clathrates extend from the surface down to the convecting portion or the input maximum depth or the point at which the dissociation temperature is exceeded, whichever is least.

In the whole-shell clathrate model, the dissociation curve is used to determine the ice shell bottom pressure based on the input T_b. Clathrate shell properties are then assessed using an initial conductive profile, then checked for convection as in standard ice Ih models.

In the underplate model, a surface heat flux q_{surf} must be assumed. This heat flux is scaled to the approximate radius of the bottom of the ice shell, then used to calculate the clathrate underplate layer thickness from the approximate thermal conductivity and the Fourier heat law (Equation 1). Because clathrate thermal conductivity is very low, most of the temperature difference across the ice shell will be across the clathrates for realistic heat fluxes for present-day icy bodies. Therefore, in this model the ice shell is assumed to be entirely conductive because the temperature difference across the overlying ice Ih layer will be too small to drive convection.

2.2 Ocean Layers

Within ocean layers, thermal energy is assumed to be transported efficiently by convection. On average, this results in a radial thermal profile that is adiabatic, *i.e.,* (Staley, 1970)

$$\frac{\partial T}{\partial P} = \frac{\alpha T}{\rho C_P}. \tag{9}$$

Unlike in the ice shell, ocean layer properties are calculated one layer at a time, with a linear pressure step $\Delta P_{\mathrm{ocean}}$ that is an input variable. The size of $\Delta P_{\mathrm{ocean}}$ sets the resolution of the ocean layer profile. At each step, starting from P_b, T_b at the bottom of

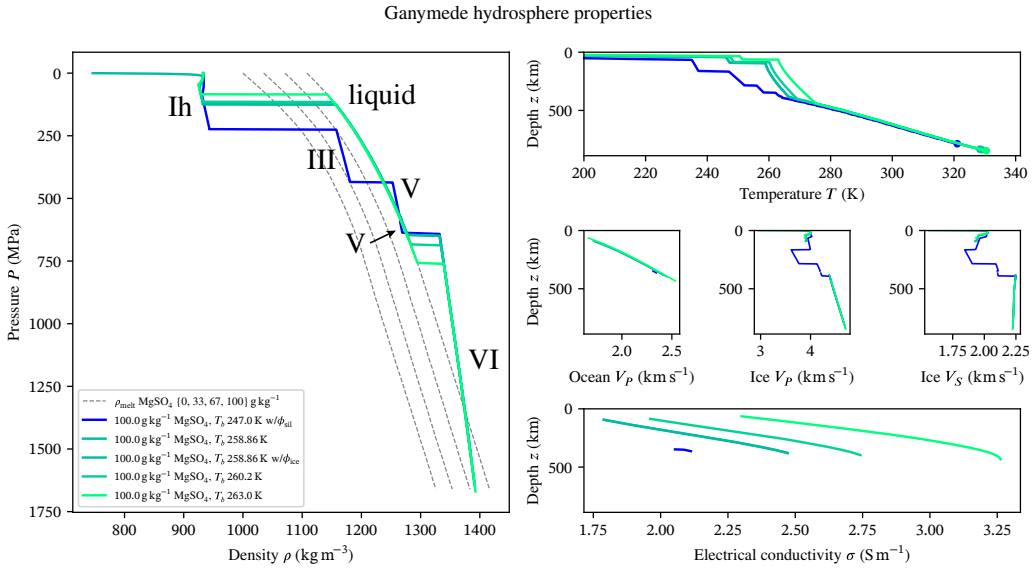

Figure 3. Plots of density vs. pressure and temperature, electrical conductivity, and sound speeds vs. depth for the hydrosphere of several models of Ganymede. Each model has an ocean with $100\,\mathrm{g\,kg^{-1}}$ $MgSO_4$(aq). Reference curves are plotted for densities at the pressure-dependent melting temperature for 0, 33, 67, and $100\,\mathrm{g\,kg^{-1}}$ $MgSO_4$. The various liquid and ice phases can be identified by jumps in the density curve. One model (blue) includes underplate ice III and V, and contains a very thin ocean because the input melting temperature is near the ice Ih–ice III–liquid triple point. This model (blue) also includes porosity modeled in rock layers (not shown; Section 2.4). A different model includes porosity modeled in ice layers ("w/ϕ_{ice}"), and exhibits a large density gradient near the surface that reflects the closure of pores due to overburden pressure.

the ice shell, the appropriate EOS for the assumed ocean solute and salinity (Table 1) is used to determine the expected phase (liquid or an ice phase). If the phase for the next P_i, T_i layer is liquid, the physical properties ρ_i, $C_{P,i}$, α_i are determined from the EOS and the next temperature $T_{i+1} = T_i + \Delta T$ is calculated using Equation 9:

$$T_{i+1} = T_i + \Delta P_{\text{ocean}} \frac{\alpha_i T_i}{\rho_i C_{P,i}}. \tag{10}$$

If the next layer is a high-pressure (HP) phase of ice, it is assumed to be undergoing vigorous two-phase convection with the ocean fluid, such that the thermal profile is set by the pressure-dependent melting temperature. This results in a steeper temperature gradient than in the liquid layers, as demonstrated in the Ganymede hydrosphere profiles displayed in Figure 3. The melting temperature for these undersea HP ices is evaluated using the EOS in the reverse of the procedure used to find P_b from T_b at the base of the ice shell (Section 2.1)—the EOS is queried with a fixed P_{i+1} for the minimum T_{i+1} at which there is a liquid phase transition. Physical properties are then determined for the appropriate ice phase EOS using *SeaFreeze*.

Because the density of some ocean liquids can be greater above the melting point, the thermal expansivity α can be negative for such liquids, creating a stably stratified layer that conducts heat rather than convecting it (Melosh et al., 2004). To account for this effect, if $\alpha < 0$ at the top of the ocean, a conductive thermal profile is assumed, with the thermal gradient set by the heat flux q_b through the ice shell and the thermal conductivity k of water (assumed to be $0.55\,\mathrm{W\,m^{-1}\,K^{-1}}$) and the Fourier heat law (Equation 1). The physical properties are evaluated step-by-step as in the convecting case, but using a smaller pressure step for the conductive layer, which is expected to be only $\lesssim$200 m thick (Melosh et al., 2004). This process is continued until $\alpha > 0$ or a phase change is reached, at which point the phase-dependent approach described above is applied. Future development plans include a self-consistent calculation of thermal conductivity for all materials (Section 2.7); currently only ice Ih has such a calculation in *PlanetProfile*.

In all cases, calculation of the physical properties with each layer from P_i and T_i also permits a determination of layer thickness using Equations 3 and 4. This process is repeated until an arbitrary threshold pressure $P_{\text{hydro,max}}$ is reached, which is set as an input. Each hydrosphere layer radius r_i is used as a starting point for possible sizes of the rock/core layers, to provide multiple options for finding a fit to the measured MoI. Therefore, $P_{\text{hydro,max}}$ must be greater than the expected pressure at the hydrosphere–

rock transition depth. $P_{\mathrm{hydro,max}}$ is intended to be set as low as possible to limit excess computation time. However, if $P_{\mathrm{hydro,max}}$ is set too low, possible sizes of rock+core layers that best match the measured MoI may be excluded from the search space, resulting in an invalid profile or one that is skewed toward one end of the MoI uncertainty bounds.

2.3 Rock and Metallic Core Layers

In order to match the total body mass and MoI self-consistently, the inner layers (those of rocks and possible core) must have their properties determined all the way to the body center for multiple starting sizes. This is because the density of the material at each layer depends on the overburden pressure and the temperature. A warmer profile will have less dense materials, requiring a larger radius for inner layers to match the total body mass, increasing those outer layers' contribution to the MoI. Conversely, a colder profile will concentrate greater densities at deeper layers within the body, resulting in a smaller MoI. Furthermore, the total heat leaving the rock portion is assumed to be equal to that escaping through the ice shell, because the ocean is assumed to convect the heat generated in the interior instantaneously on geologic timescales. This adds a dependence on the hydrosphere layer profile to the thermal profiles modeled in the inner layers. For waterless bodies, the surface heat flux is an input quantity and variation for matching the MoI is achieved by varying the porosity.

In both rock and core layers, physical properties are evaluated by interpolating P–T EOS data tables generated by *Perple_X* (Connolly, 2009). The *Perple_X* software calculates physical properties of mineral assemblages based on an input chemical composition by Gibbs free energy minimization. For rocks, we have generated lookup tables for chemical compositions over P and T conditions relevant to solar system moons based on chondritic and cometary material that has partially differentiated, such that free fluids have been lost to the ocean or to space, but volatile-bearing and volatile-free minerals, dense iron, and siderophile elements are retained. In the current version of *PlanetProfile*, only solid phases are modeled, although implementing self-consistent melt for rock and metallic layers is in progress (Section 2.7).

Chondrite types CI, CM, and CV are included (elemental composition from Lodders and Fegley (1998) and Lodders (2021)), as is a composition consistent with Comet 67P/C–G (based on combining: Filacchione et al. (2019); Bardyn et al. (2017); Le Roy et al. (2015);

Pätzold et al. (2016); Dhooghe et al. (2017)). Additionally, for CM chondrites, we include a fully differentiated composition relevant to Ganymede based on an estimated metallic core size and an input sulfur sequestration, from 0 wt% S to 20 wt% S in the core. The maximum of these is the approximate total sulfur that a bulk-CM-chondrite Ganymede could lose to the core if the primordial sulfur content were all sequestered in the core.

In rock layers, a conductive thermal profile is assumed. This is not a good approximation for bodies like Io, where the surface heat flux can be over $2\,\mathrm{W\,m^{-2}}$ (Lainey et al., 2009). However, MoI-matching density profiles for rocks may be found for heat fluxes about 10% of this rate. An implementation for self-consistent convection modeling in rocks is being developed (Section 2.7). Application to Io is discussed further in Section 4.

For the conductive thermal profile in rocks, the Fourier heat law can be integrated to obtain an expression accounting for internal heating (Turcotte & Schubert, 2002):

$$T_{\mathrm{bot}} = T_{\mathrm{top}} + \frac{H_{\mathrm{tot}}}{6k}\left(r_{\mathrm{top}}^2 - r_{\mathrm{bot}}^2\right) + \left(\frac{q_{\mathrm{top}} r_{\mathrm{top}}^2}{2k} - \frac{H_{\mathrm{tot}} r_{\mathrm{top}}^3}{6k}\right)\left(\frac{1}{r_{\mathrm{bot}}} - \frac{1}{r_{\mathrm{top}}}\right), \tag{11}$$

$$H_{\mathrm{tot}} = H_{\mathrm{tidal}} + \rho_{\mathrm{rad}} Q_{\mathrm{rad}},$$

where T_{bot}, T_{top}, r_{bot}, r_{top} are the temperatures and radii at the bottom and top of the discrete layer, k is thermal conductivity, q_{top} is the heat flux leaving the top surface of the layer, H_{tidal} is the volumetric heating (from tidal forces) in $\mathrm{W\,m^{-3}}$, ρ_{rad} is the density of materials contributing radiogenic heating, and Q_{rad} is the radiogenic heating rate in $\mathrm{W\,kg^{-1}}$. All quantities are in SI units. In *PlanetProfile*, fixed tidal heating and radiogenic heating rates are assumed as inputs. Self-consistent calculation of tidal heating rates throughout the interior is in development, using a Python adaptation of the *ALMA3* package (Spada, 2008), *PyALMA* (Section 2.7).

Rock layer properties are evaluated all the way from each starting hydrosphere layer radius down to the center of the body. To save on computational overhead, the default behavior is to begin this profile search starting from each ocean layer. If a mass-matching profile is not found, the profile search is restarted from the surface to account for bodies that may be fully frozen. A fixed number of layers n_{sil} sets the profile resolution in this region, and a linear step in radius is now used. Many of these hydrosphere+rock profiles will exceed the body mass; those that do are immediately discarded. For the remaining profiles, the method of matching the MoI varies depending on whether or not a core is intended to be modeled. When no core is modeled, the profile with greatest mass that

is less than the total body mass is retained as a candidate for MoI matching, the vacuum porosity ϕ_{rock} is increased, and the process is repeated for n_ϕ total profiles over a range of ϕ_{rock} values.

2.3.1 Metallic Core Layers

When a core is modeled, the core layers are handled last as they are at the center of the body. As described above, physical properties of core layers are evaluated by interpolating *Perple_X* data tables using the thermodynamic data of Saxena and Eriksson (2015). We have generated *Perple_X* tables for core compositions ranging from pure iron (100 wt% Fe) to the maximum core sulfur content of ∼35 wt% S (100 wt% FeS) in 5 wt% S increments, resulting in a single 3D data table in P–T–x_{FeS}. This 3D table is interpolated based on an input core sulfur mixing ratio x_{FeS} to obtain a P–T EOS for the core material.

The core layers must now be evaluated. First, a maximum core size is set based on a minimum density $\rho_{\text{core,min}}$ below that expected (*e.g.,* 4500 kg m^{-3}, the density of FeS at ∼2.6 GPa and 1350 K). The maximum core size is that consistent with an amount of innermost rock layers replaced by core material with a density $\rho_{\text{core,min}}$, such that the total mass is just less than the measured body mass. Similar to starting the rock profile search from each ocean layer by default, this maximum core size is used to reduce computational overhead, by reducing the number of core profiles to iterate over.

Next, the rock layers with outer boundaries inside the maximum core radius are each used as a starting point for the core layer profiles. A linear step in radius is used, and for a fixed number of layers n_{core} the thermal profile is assumed to be adiabatic (Equation 9). Physical properties are calculated from the top down, one core layer at a time, starting from the pressure, temperature, and local gravity at the top of the first rock layer replaced. The local gravity for each core layer is modeled as proportional to radius, which is only true for a constant density sphere, but the density typically changes very little across core layers because of the adiabatic assumption. The core profile search operation is performed in a vectorized fashion across each rock profile. Finally, the single core profile for each rock profile that is the greatest mass less than the total body mass is selected as the best fit. This gives a set of mass-matching core+rock profiles, from among which the best-fit MoI is selected as the model output (Section 2.3.2).

A toggle is included to skip the self-consistent rock layer calculation, and instead use a uniform density for both rocks and core. In this case, the core density is assumed as an input and the core size is scaled to match the total body mass. This option is included to match the behavior of previous versions of the software (*e.g.,* Vance et al., 2018) and for faster operation in large parameter-space searches.

For bodies like Io where no surface water is modeled, there is only one radius available for the rock profile search. Whether a core is modeled or not, the rock vacuum porosity $\phi_{\rm rock}$ is varied over an input range as in the case where no core is modeled. When a core is modeled, the core profile search algorithm is the same as for models with a hydrosphere—only the mass-matching rock+core profile for each value of $\phi_{\rm rock}$ is carried forward to the MoI-matching calculation.

2.3.2 Matching the MoI

Once the set of mass-matching, full-body profiles has been generated, they are each compared to the MoI to determine which best matches. As the profiles are spherically symmetric, each layer's contribution to the total axial moment of inertia C is

$$\Delta C_i = \frac{8\pi}{15}\rho_i \left(r_i^5 - r_{i+1}^5\right), \tag{12}$$

with the final radius $r_{n_{\rm tot}+1} = 0$ at the center of the body and $C = \sum \Delta C_i$. This expression follows from the uniform-density layers in our model and the moment of inertia definition (*e.g.,* Morin, 2008)

$$C = \int_M s^2 dm, \tag{13}$$

where s is the distance between each dm and the axis of rotation associated with C.

The profile with the MoI closest to the measured value is highlighted as the best match to the inputs and assumptions. Several bulk properties are calculated at this stage, such as the mean rock density, thickness of the ocean layer, total mass of dissolved salts, *etc.* Several of these properties are compared among the other profiles that fit within the input uncertainty for the MoI in order to estimate the range of uncertainty in these quantities. The individual layer properties for only the best-match profile are retained for the final processing steps and for saving to disk.

2.4 Porosity in Rock and Ice Layers

PlanetProfile supports modeling of porosity in rock and ice layers (independent of one another). These features can optionally be enabled for any model, and porosity in rock layers is required for self-consistent modeling of bodies with no metallic core or hydrosphere. Porosity in any material follows the same general framework (Han et al., 2014):

$$\phi(P) = \phi_{\text{vac}} \exp\left\{-\frac{cP}{P_c}\right\}, \tag{14}$$

where $\phi(P)$ is the volume fraction of void space within the matrix as a function of pressure, ϕ_{vac} is the porosity of the material if there were no overburden pressure (extrapolated for materials like ice III that are not stable at low pressures), c is a constant (6.15), and P_c is an experimentally derived pore closure pressure, beyond which pores are effectively eliminated ($\phi < 0.2\%$).

Based on other characteristics of the model, the pore space is assumed to be evacuated or filled with other materials. In ices near the surface, and in rocks for bodies with no hydrosphere, pores are assumed to be evacuated. Within HP ices found within ocean fluids, the pore space is assumed to be filled with ocean fluid. Because these layers are assumed to be at the melting temperature, both ice and fluid are stable and the ocean EOS is used to determine pore fluid properties. Within porous rocks beneath a hydrosphere, the pores are assumed to be filled with ocean fluids, and the ocean EOS and pore-space P and T conditions are used to determine the phase and properties of the pore material. Pore materials are assumed to have the same temperature as the matrix in which they are embedded.

When the pore material is liquid, the matrix material is assumed to rigidly support the overburden pressure, such that the pore space pressure increases based on the local gravity and the overburden pressure of only the pore material. Pore spaces are assumed to be sufficiently permeable as to communicate these pressures vertically. The pore pressure is assumed to provide a counteracting force that acts to hold pores open, ultimately resulting in a net effective pressure P_{eff} in Equation 14 that determines the porosity (Vitovtova et al., 2014):

$$P_{\text{eff}} = P_m - \alpha_{\text{eff}} P_f, \tag{15}$$

where P_m is the overburden pressure for the matrix material, P_f is the pressure within the pore fluid, and α_{eff} is a constant that characterizes the behavior of the matrix. In *PlanetProfile*, α_{eff} is a variable, by default set to 0.95 after Vitovtova et al. (2014).

Physical properties of the pore and matrix materials are combined to get bulk layer properties using the two-phase composite model of Yu et al. (2016):

$$M^J = (1-\phi)M_f^J + \phi M_m^J, \tag{16}$$

where M_m and M_f stand for a mechanical property for the matrix and pore fluid respectively, M is the same mechanical property for the combined two-phase layer, and J is a mixing parameter that depends on the character of pores and the mechanical property. Considering two-phase porous materials, J typically ranges from 0 to 1, and can be greater than 1 for seismic velocities in some materials (Yu et al., 2016). For several properties, such as density ρ, $J = 1$ and Equation 16 describes an arithmetic mean, weighted by ϕ. In *PlanetProfile*, a J value for each layer property is set independently, for porous rock and ice separately; we assume $J = 1$ for all properties except the seismic properties:

$$\text{Bulk modulus: } J_{K_S} = 0.35$$

$$\text{Shear modulus: } J_{G_S} = 0.35$$

$$\text{P-wave speed: } J_{V_P} = 0.75$$

$$\text{S-wave speed: } J_{V_S} = 0.85.$$

These values are selected as rough "middle" estimates from the mineral assemblages studied by Yu et al. (2016). If these values are known for a specific assumed mantle composition, each J should be updated to the known value for self-consistency.

2.5 Seismic and Electrical Properties

Seismic and electrical properties for each layer profile are calculated from P, T, and ϕ conditions for each layer after the entire self-consistent physical structure has been determined. Seismic properties are determined from the EOS (Table 1); for some materials, such as methane clathrates, the P–T dependence of the seismic properties is implemented separately from other physical properties. Output files formatted for compatibility with the open-source packages *AxiSEM* (Nissen-Meyer et al., 2014) and *Mineos* (`https://github.com/geodynamics/mineos`) are printed at the end of each model run. Past studies (*e.g.,* Stähler et al., 2018) have paired previous versions of *PlanetProfile* with *AxiSEM* to understand how seismic data may aid in constraining the interior structure of icy moons. The *TauP* package (Crotwell et al., 1999) implemented in the open-source

ObsPy framework (Beyreuther et al., 2010) provides complementary calculations for seismic travel times; integration with this package is a work-in-progress. Calculated seismic and physical properties can also be passed to gravitational modeling software such as *ALMA3* (Section 2.7), for example in iterative modeling that evaluates tidal heating self-consistently.

Depth-dependent electrical properties are critical for magnetic sounding investigations that connect magnetic measurements to interior structure (Vance et al., 2021). On global scales, conductivity of ice ($\sim 10^{-5}\,\mathrm{S\,m^{-1}}$, Petrenko & Schulson, 1992), clathrate ($\sim 10^{-5}\,\mathrm{S\,m^{-1}}$, Stern et al., 2021), and rock matrix materials ($\lesssim 10^{-7}\,\mathrm{S\,m^{-1}}$, Glover & Vine, 1994) are expected to be negligible for the hours-long oscillations of planetary magnetic fields. In *PlanetProfile*, we set the conductivity of many of these materials to an arbitrarily small value ($10^{-8}\,\mathrm{S\,m^{-1}}$). Metallic core layers are expected to have a high conductivity ($\sim 10^{6}\,\mathrm{S\,m^{-1}}$, Pozzo et al., 2012), so we set them to an arbitrarily large value ($10^{6}\,\mathrm{S\,m^{-1}}$).

For the ocean and pore-filling fluids, electrical conductivity is determined from empirical models, interpolation, and/or extrapolation of available laboratory measurements (Table 1). Pure water conductivity is set to a constant $\sigma = 10^{-5}\,\mathrm{S\,m^{-1}}$ (Light et al., 2004), as even dilute ions will dominate the electrical properties (*e.g.,* Quist & Marshall, 1968) and pure water oceans will probably not persist over geologic time scales as materials dissolve into the fluid. Seawater conductivity is determined as a function of P, T, and salinity w using the Python implementation of the *Gibbs Seawater* package (McDougall & Barker, 2011). Following Vance et al. (2018), conductivity of $MgSO_4$(aq) ocean fluids is determined by interpolation of measurements at relevant conditions from Larionov and Kryukov (1984). The laboratory measurements these implementations are based on were necessarily limited. For $MgSO_4$ oceans, the data are extrapolated above $1.2\,\mathrm{g\,kg^{-1}}$, below 298 K, and above 784 MPa. This extrapolation is justified by smooth functional behavior and the expected physical dependence (Vance et al., 2018). The need for extrapolation underscores the critical importance of future laboratory measurements of electrical conductivities for solutions at P and T conditions that are relevant to ocean worlds.

2.6 Magnetic Induction Properties

To determine properties of the induced magnetic field from each body, *PlanetProfile* makes use of the open-source Python framework *MoonMag* (Styczinski, Vance, Harnett, & Cochrane, 2022). *MoonMag* calculates induced magnetic fields from a description of the excitation moments, the radial conductivity profile, and the shape of asymmetric conducting boundaries in terms of spherical harmonic coefficients. Excitation moments are the amplitudes, phases, and periods of oscillation for each vector component of the time-varying magnetic field applied to the body. The excitation moments must be estimated or determined from planetary magnetospheric models. *PlanetProfile* uses excitation moments calculated using Fourier methods (Vance et al., 2021). SPICE kernels are used to evaluate the moons' locations and planet orientation. Combined with planetary field models detailed in the literature, the magnetic field is evaluated at the body in a time series that is inverted to obtain the excitation moments.

The induced field is determined by a recursive layer method (Styczinski, Vance, Harnett, & Cochrane, 2022), where each layer has uniform conductivity. The time required to calculate the induced field is linear in the number of conducting layers for symmetric models, so the conductivity profile is contracted before being passed to *MoonMag*. All adjacent layers with conductivity below or above threshold values are combined into a single low- or high- conductivity layer. Layers such as those in the ocean with conductivities between this range may optionally be reduced to a fixed number of interpolated layers (default 5). The depth dependence of conductivity within ocean layers has significant effects on the induced magnetic moments (Vance et al., 2021); we consider this approach to be an acceptable compromise between uniformly conducting oceans and those with excessively high spatial resolution, given other model uncertainties and approximations.

MoonMag, and its implementation within *PlanetProfile*, also supports asymmetric boundary shapes. All large moons in the solar system rotate synchronously, so each has substantial J_2 and C_{22} gravity coefficients, describing oblateness and elongation, respectively. Therefore, some asymmetric shape is expected from orbital motion and gravity alone. For most moons, the gravity coefficients contribute half or more of the expected difference from asymmetric layers (Styczinski, Vance, Harnett, & Cochrane, 2022). Asymmetric models can add substantial computation time, so for most bodies only gravity co-

efficients are considered. For some bodies, such as Enceladus, the ocean is known to have an asymmetric interface with the ice shell (Hemingway & Mittal, 2019); for such bodies, the induced field is significantly affected and example asymmetric shapes are included with the default model (Section 3).

Several helpful features are wrapped from or re-implemented based on *MoonMag*, including evaluating the induced magnetic field at points on the surface or along a spacecraft trajectory relative to the body. Also implemented are a number of helper functions for generating or evaluating parameter-space searches and statistical analyses. For example, functions to create "induct-o-gram" plots vary two relevant parameters affecting ocean properties such as a fixed ("silicate") rock density ρ_{rock} and salinity w over some range for each. The induced field at the magnetic pole is then evaluated over a grid of values for each parameter and contours of the field strength are plotted (Figure 4). This has an advantage over canonical induct-o-gram plots (*e.g.,* Khurana et al., 2002) with uniform ocean conductivity $\overline{\sigma}$ and total ocean layer thickness D, as $\overline{\sigma}$ and D are not independent in self-consistent models. For Bayesian methods involving a parameter adjustment between each model run—*e.g.,* finding maximum likelihood for model parameters based on a fit to magnetometer data—individual model runs can be chained together with a helper function (`UpdateRun`). This function recalculates only those portions of the prior self-consistent model solution that will be affected by the desired parameter update, saving computation time.

2.7 Directions for Future Development

PlanetProfile is in active development. A number of updates are planned or in-progress that are intended to improve on the self-consistency of the models and their utility in scientific applications. Improvements in progress include:

1. Convection in rocks. Models are currently limited to conductive thermal profiles in rock layers, which will only be realistic for bodies without significant internal heating.
2. Including metallic core and rock melt fraction from *Perple_X*. The *Perple_X* tables currently implemented in *PlanetProfile* for the EOS for rock and core materials include only the properties of the solid matrix, even when molten rocks are present.

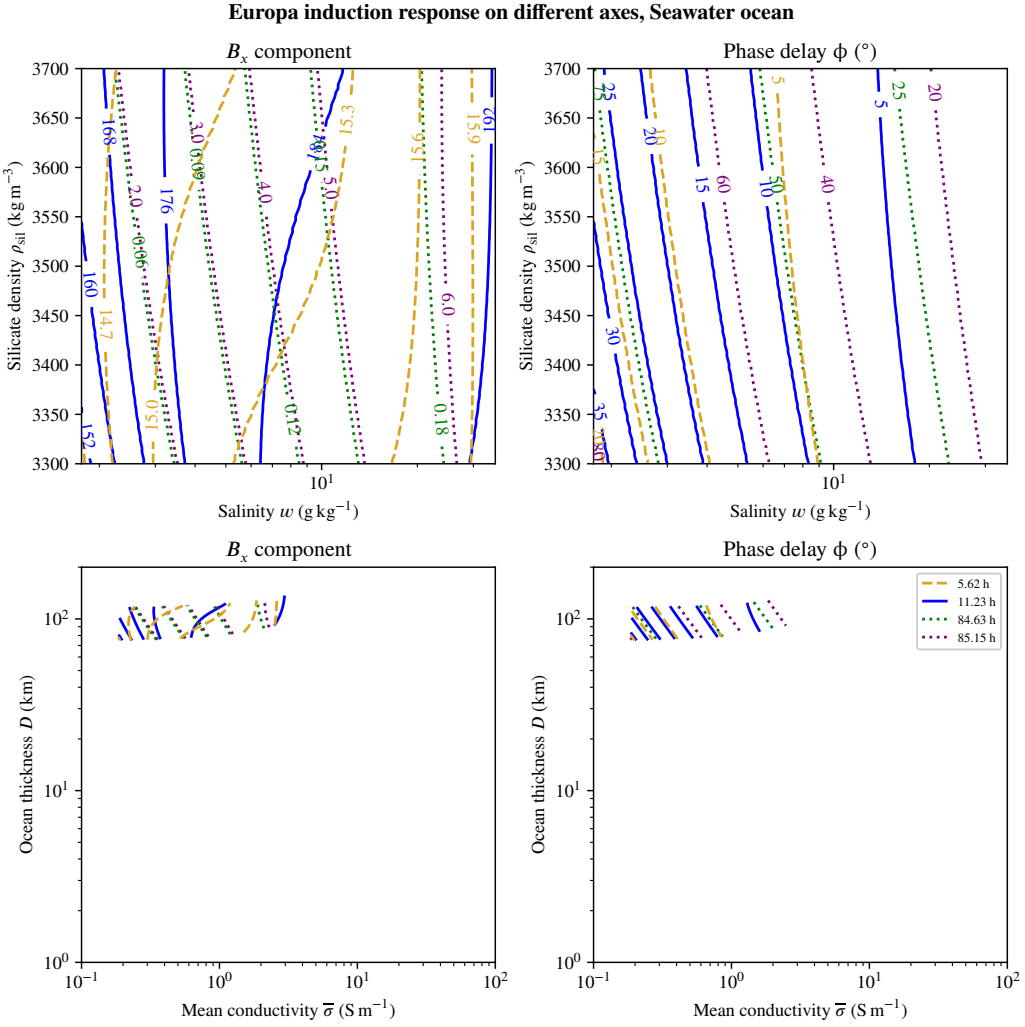

Figure 4. Induct-o-gram showing the induction response strength and phase delay in the B_x component for Europa (IAU coordinates) at the moving magnetic pole relative to several body properties. Model inputs are the axes on the top two panels, a fixed ("silicate") rock density ρ_{rock} and Seawater salinity w. The bottom two panels show the same contours as the top, but plotted against the mean conductivity $\overline{\sigma}$ and total ocean thickness D of the self-consistent models. The range of values shown for $\overline{\sigma}$ and D is consistent with past studies (*e.g.,* Zimmer et al., 2000; Khurana et al., 2002; Vance et al., 2021), demonstrating that such a wide parameter space is likely not necessary to consider when further constraints are included.

3. Self-consistent rock layers with variable iron and sulfur differentiation. The total elemental content of a body is limited by its primordial abundances. Since we assume a chondritic or cometary origin, the iron and sulfur content in the core is dependent on how much can be extracted from the rocks, and the total budget in both sources should be consistent with the assumed parent material.
4. Self-consistent tidal heating with *PyALMA*, including iterative profile evaluation. An in-progress Python implementation of *ALMA3* (Melini et al., 2022), called *PyALMA*, supports the calculation of gravitational Love numbers from standard *PlanetProfile* output files. The tidal Love numbers h_2 and k_2 describe the response of a body to gravitational forcing and can be used to derive tidal heating rates, but themselves depend on the material properties. Self-consistency of *PlanetProfile* models can be improved by using *PyALMA* to calculate Love numbers following a model run, then calculating tidal heating rates from the Love numbers and using these rates as inputs to a second model iteration. This process can then be repeated until the model converges. h_2 and k_2 are also indirectly observable through gravity and geodetic measurements, providing additional means of constraining interior structure from *PlanetProfile* models.
5. Integration with the *TauP* package. Calculation of seismic wave travel times will provide an additional connection between interior structure model outputs and measurements available to spacecraft.

Improvements planned for the future include:

1. Self-consistent thermal profile in ice, including tidal heating and T_b values derived from surface heat flux. The initial thermal profile in the ice shell is determined from the assumed ocean melting temperature and the assumption of a $1/T$ dependence for the ice thermal conductivity k. A more self-consistent method is desirable, and converting the assumptions required to an input surface heat flux is one way to resolve this issue.
2. Improved convection parameterization in ice. Convection in the ice shell is modeled after Deschamps and Sotin (2001). The fit parameters for this model were derived for a specific case with no tidal heating. Implementing a convection model that accounts for tidal heating would improve self-consistency.

3. P- and T-dependent calculations of k for all materials. Thermal conductivity k is calculated as a function of T only, and only for ice layers. For all other materials, k is set to a constant. Especially for conductive profiles in rock layers, this approximation limits the range of validity of the models.
4. More options for ocean fluids, as they become implemented in *SeaFreeze*. A wide variety of solutes are possible and likely to be found in subsurface oceans of icy moons. Notably absent from the EOS data currently implemented in *PlanetProfile* is ammonia (NH_3), which is expected to be common in the outer solar system and likely contributes significantly to ocean properties (Choukroun & Grasset, 2010; Kimura & Kamata, 2020). A wider range of supported fluids is expected to be implemented in *SeaFreeze* as more laboratory measurements become available.
5. Time-dependent models. *PlanetProfile* models assume the body is in steady-state, *i.e.,* the heat flux entering and leaving each layer is equal and no melting or freezing is actively occurring. If this assumption were to be relaxed, *PlanetProfile* models could be used as a starting point for projecting forward or backward in time to study the evolution of terrestrial bodies.

3 Model Results Across the Outer Solar System

PlanetProfile is designed to be versatile in allowing for investigation of a wide variety of assumed input properties. To serve as a starting point from which to iterate, *PlanetProfile* comes packaged with a default model for each major moon in the solar system and Pluto. After the package is installed or cloned from the GitHub repository, an installation function copies default models to the working directory so they can be easily accessed and edited by the user. These models represent a synopsis of measured and estimated characteristics for each body based on the available literature and features implemented in *PlanetProfile*.

Tables 5 – 9 describe major layer properties calculated for each default model using *PlanetProfile*. Figures 5 – 9 show "wedge" diagrams representing the material layers described in the corresponding tables. These figures and tables (LaTeX source) are output directly by the software. We have grouped together the output summary tables and figures by size to show greater detail in the wedge diagrams for smaller bodies. Tables 10 – 13 contain the major input parameters for each model along with references to sources from the literature. Text files containing the full model outputs are available as

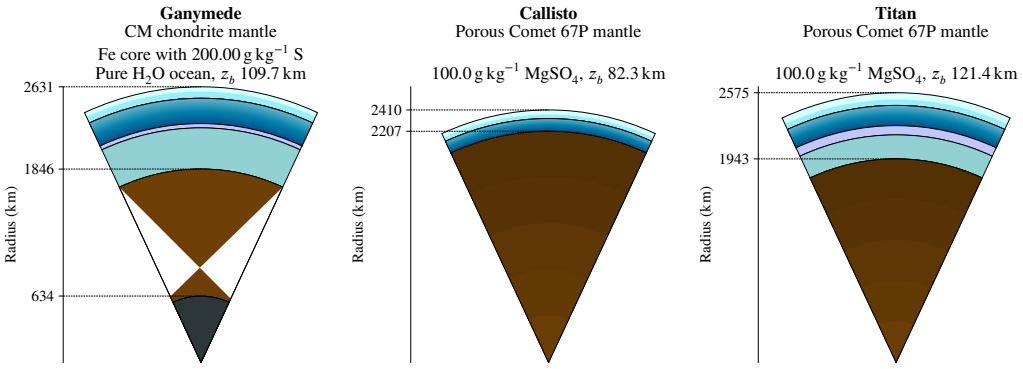

Figure 5. Wedge diagram showing major material layers for default models of the largest moons: Ganymede, Callisto, and Titan, to scale. The depicted models are as summarized in Table 5. Conducting ice Ih, at the surface of each body, is shown in pale blue; convecting ice Ih, which is present for all of these models, is cyan; ocean layers are blue with a color gradient; ice V is lavender; ice VI is gray-green; rock is brown, and porous rock is shown with a color gradient; metallic core layers are dark gray.

a Zenodo archive: `https://doi.org/10.5281/zenodo.7250785`. These files each list the hundreds of individual layers that make up the profile, along with the material type and physical properties. A number of header lines also describe bulk properties and selected input parameters.

4 Discussion

Geophysical models applied in planetary science typically either focus on large-scale material layers with uniform properties or smaller-scale, more detailed dynamical modeling that cannot easily be scaled to a global context. *PlanetProfile* represents a compromise between these extremes. Spherical symmetry allows models to be run quickly, while still capturing major global-scale processes. Application of scaling laws from more detailed studies and EOS data from laboratory measurements over many individual layers affords much greater fidelity between required assumptions and results of the model than is possible in simpler approaches. To our knowledge, the only comparable software available is *BurnMan* (Cottaar et al., 2014), but *BurnMan* focuses on Earth-like interiors and is not intended for application to icy bodies with subsurface oceans.

Table 5. *PlanetProfile* output summary table for default models of the largest moons: Ganymede, Callisto, and Titan. Material layers are depicted in Figure 5. M: total body mass; C: axial moment of inertia; R: outer radius of layer; $\rho_{\mathrm{rock,mean}}$: mean density of rock layers, including pore fluids; T_b: temperature at bottom of ice shell; q_{surf}: surface conductive heat flux; q_{con}: heat flux through ice shell at the bottom of the conductive layer; η_{con}: ice viscosity for possible convecting region based on Deschamps and Sotin (2001) approach; D_{Ih}, D_{V}, D_{VI}: thickness of ice layers; D_{ocean}: thickness of contiguous liquid water ocean layer; $\overline{\sigma}_{\mathrm{ocean}}$: mean conductivity across contiguous ocean layers (each linear pressure step is weighted uniformly); ϕ_{rock}: vacuum porosity of rocks. Upper and lower uncertainty values on C_{model}/MR^2 results represent the next nearest models. A zero value indicates that no valid model lies between the best match and the uncertainty bounds of the input C/MR^2 value.

	Ganymede	**Callisto**	**Titan**
Ocean comp.	Pure H_2O	100.0 g kg^{-1} $MgSO_4$	100.0 g kg^{-1} $MgSO_4$
M (kg)	1.4819×10^{23}	1.0759×10^{23}	1.3452×10^{23}
M_{model} (kg)	1.4819×10^{23}	1.0756×10^{23}	1.3447×10^{23}
C/MR^2	0.3115 ± 0.0028	$0.3549^{+0.0042}_{-0.0148}$	$0.341^{+0.010}_{-0.020}$
C_{model}/MR^2	$0.31143^{+0.00023}_{-0.00025}$	$0.34121^{+0.00000}_{-0.00000}$	$0.32143^{+0.00000}_{-0.00022}$
$\rho_{\mathrm{rock,mean}}$ (kg m^{-3})	3237	2066	2795
T_b (K)	258.86	262.0	255.0
q_{surf} (mW m^{-2})	16.3	18.3	12.4
q_{con} (mW m^{-2})	17.7	19.6	13.6
η_{con} (Pa s)	5.89×10^{14}	5.35×10^{14}	8.48×10^{14}
D_{Ih} (km)	109.7	82.3	121.4
D_{ocean} (km)	241.2	121.3	192.7
D_{V} (km)	40.9	-	88.2
D_{VI} (km)	393.2	-	229.3
$\overline{\sigma}_{\mathrm{ocean}}$ (S m^{-1})	0.0	2.4	1.4
R_{surf} (km)	2631.2	2410.3	2574.7
R_{rock} (km)	1846.1	2206.7	1943.1
R_{core} (km)	633.8	-	-
ϕ_{rock}	-	0.90	0.90

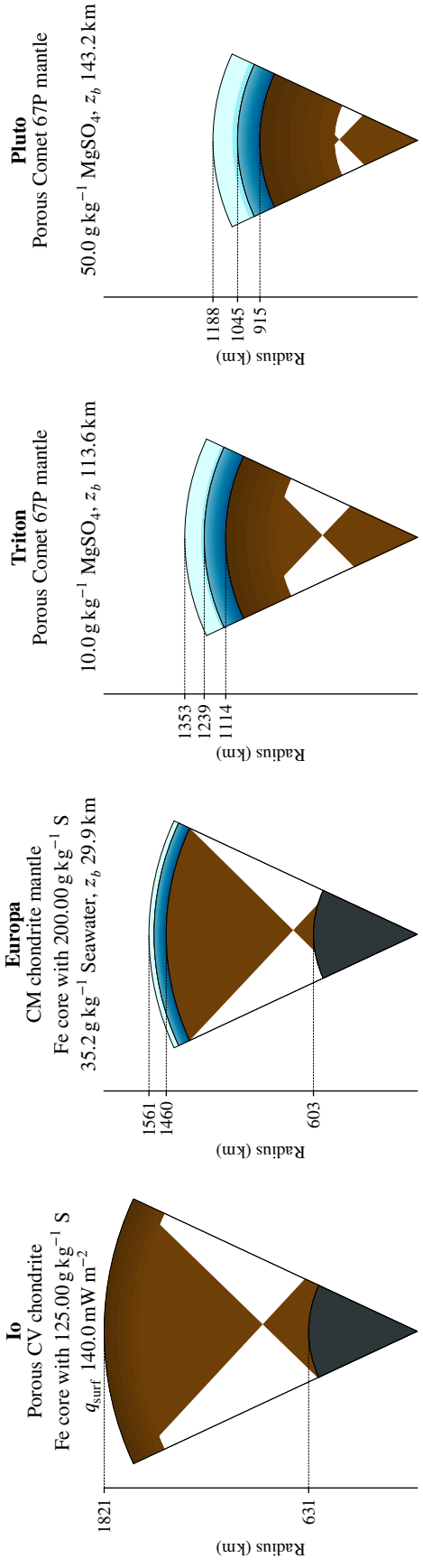

Figure 6. Wedge diagram showing major material layers for default models of large moons Io, Europa, and Triton with similarly-sized Pluto, to scale. The depicted models are as summarized in Table 6; layer colors are indicated as described in Figure 5.

Table 6. *PlanetProfile* output summary table for default models of large moons Io, Europa, and Triton with similarly-sized Pluto. Material layers are depicted in Figure 6. Variable definitions are as in Table 5.

	Io	**Europa**	**Triton**	**Pluto**
Ocean comp.	No H_2O	$35.2\,\mathrm{g\,kg^{-1}}$ Seawater	$10.0\,\mathrm{g\,kg^{-1}}$ $MgSO_4$	$50.0\,\mathrm{g\,kg^{-1}}$ $MgSO_4$
M (kg)	8.9320×10^{22}	4.8000×10^{22}	2.1410×10^{22}	1.3030×10^{22}
M_{model} (kg)	8.9251×10^{22}	4.7986×10^{22}	2.1408×10^{22}	1.3028×10^{22}
C/MR^2	0.37685 ± 0.00035	0.346 ± 0.005	0.31 ± 0.03	0.31 ± 0.03
C_{model}/MR^2	0.37688	$0.34593^{+0.00038}_{-0.00037}$	$0.32916^{+0.00004}_{-0.00000}$	$0.32028^{+0.00006}_{-0.00000}$
$\rho_{\mathrm{rock,mean}}$ ($\mathrm{kg\,m^{-3}}$)	3404	3287	2908	2863
T_b (K)	-	268.305	266.0	265.0
q_{surf} ($\mathrm{mW\,m^{-2}}$)	140.0	16.0	11.6	9.5
q_{con} ($\mathrm{mW\,m^{-2}}$)	-	16.7	13.8	12.2
η_{con} (Pa s)	-	3.49×10^{14}	2.92×10^{14}	3.30×10^{14}
D_{Ih} (km)	-	29.9	113.6	143.2
D_{ocean} (km)	-	70.9	125.1	129.9
$\overline{\sigma}_{\mathrm{ocean}}$ ($\mathrm{S\,m^{-1}}$)	-	2.8	0.3	1.4
R_{surf} (km)	1821.5	1560.8	1352.6	1188.3
R_{rock} (km)	1821.5	1460.0	1113.9	915.2
R_{core} (km)	631.4	603.5	-	-
ϕ_{rock}	0.70	-	0.35	0.35

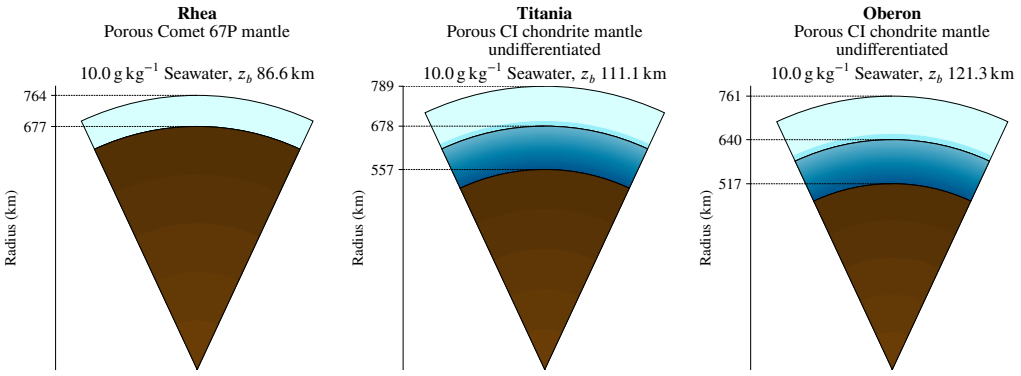

Figure 7. Wedge diagram showing major material layers for default models of mid-sized moons Rhea, Titania, and Oberon, to scale. The depicted models are as summarized in Table 7; layer colors are indicated as described in Figure 5.

Table 7. *PlanetProfile* output summary for default models of mid-sized moons Rhea, Titania, and Oberon. Material layers are depicted in Figure 7. Variable definitions are as in Table 5.

	Rhea	**Titania**	**Oberon**
Ocean comp.	10.0 g kg^{-1} Seawater	10.0 g kg^{-1} Seawater	10.0 g kg^{-1} Seawater
M (kg)	2.3065×10^{21}	3.5270×10^{21}	3.0140×10^{21}
M_{model} (kg)	2.2994×10^{21}	3.5260×10^{21}	3.0103×10^{21}
C/MR^2	0.3721 ± 0.0036	0.306 ± 0.03	0.307 ± 0.03
C_{model}/MR^2	$0.37132^{+0.00000}_{-0.00000}$	$0.31097^{+0.00004}_{-0.00000}$	$0.31035^{+0.00007}_{-0.00000}$
$\rho_{\mathrm{rock,mean}}$ (kg m^{-3})	1364	3071	3058
T_b (K)	265.0	269.4	269.4
q_{surf} (mW m^{-2})	2.8	10.4	9.6
q_{con} (mW m^{-2})	9.4	14.1	13.5
η_{con} (Pa s)	3.58×10^{14}	2.66×10^{14}	2.66×10^{14}
D_{lh} (km)	86.6	111.1	121.3
D_{ocean} (km)	0.0	120.8	122.7
$\overline{\sigma}_{\mathrm{ocean}}$ (S m^{-1})	-	0.9	0.9
R_{surf} (km)	763.5	788.9	761.4
R_{rock} (km)	676.9	557.0	517.4
ϕ_{rock}	0.92	0.10	0.10

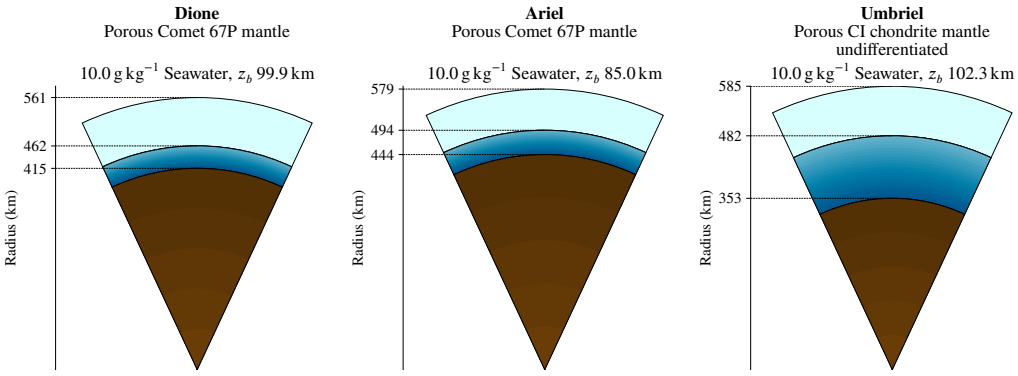

Figure 8. Wedge diagram showing major material layers for default models of small moons Dione, Ariel, and Umbriel, to scale. The depicted models are as summarized in Table 8; layer colors are indicated as described in Figure 5.

Table 8. *PlanetProfile* output summary for default models of small moons Dione, Ariel, and Umbriel. Material layers are depicted in Figure 8. Variable definitions are as in Table 5.

	Dione	**Ariel**	**Umbriel**
Ocean comp.	10.0 g kg^{-1} Seawater	10.0 g kg^{-1} Seawater	10.0 g kg^{-1} Seawater
M (kg)	1.0954×10^{21}	1.3530×10^{21}	1.1720×10^{21}
M_{model} (kg)	1.0946×10^{21}	1.3526×10^{21}	1.1696×10^{21}
C/MR^2	0.33 ± 0.01	0.306 ± 0.03	0.319 ± 0.03
C_{model}/MR^2	$0.33005^{+0.00088}_{-0.00067}$	$0.32603^{+0.00042}_{-0.00000}$	$0.31893^{+0.00052}_{-0.00008}$
$\rho_{\mathrm{rock,mean}}$ (kg m^{-3})	2246	2526	2894
T_b (K)	270.93	270.93	270.93
q_{surf} (mW m^{-2})	9.6	5.2	4.4
q_{con} (mW m^{-2})	14.2	7.1	6.4
η_{con} (Pa s)	2.56×10^{14}	2.45×10^{14}	2.45×10^{14}
D_{lh} (km)	99.9	85.0	102.3
D_{ocean} (km)	46.3	50.2	129.0
$\overline{\sigma}_{\mathrm{ocean}}$ (S m^{-1})	0.9	0.9	0.9
R_{surf} (km)	561.4	578.9	584.7
R_{rock} (km)	415.2	443.7	353.4
ϕ_{rock}	0.50	0.35	0.10

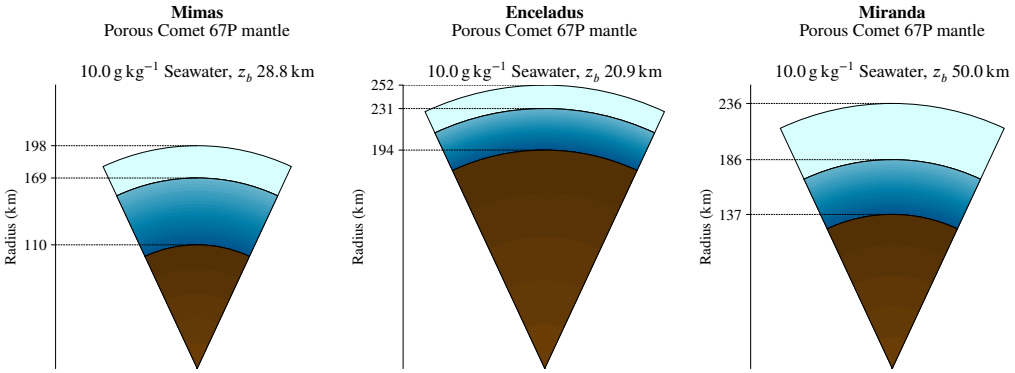

Figure 9. Wedge diagram showing major material layers for default models of the smallest large moons: Mimas, Enceladus, and Miranda, to scale. The depicted models are as summarized in Table 9; layer colors are indicated as described in Figure 5.

Table 9. *PlanetProfile* output summary for default models of the smallest large moons: Mimas, Enceladus, and Miranda. Material layers are depicted in Figure 9. Variable definitions are as in Table 5.

	Mimas	**Enceladus**	**Miranda**
Ocean comp.	10.0 g kg^{-1} Seawater	10.0 g kg^{-1} Seawater	10.0 g kg^{-1} Seawater
M (kg)	3.7493×10^{19}	1.0802×10^{20}	6.5900×10^{19}
M_{model} (kg)	3.7423×10^{19}	1.0777×10^{20}	6.5866×10^{19}
C/MR^2	0.355 ± 0.01	0.335 ± 0.001	0.35 ± 0.03
C_{model}/MR^2	$0.35487^{+0.00086}_{-0.00041}$	$0.33489^{+0.00000}_{-0.00020}$	$0.34500^{+0.00000}_{-0.00048}$
$\rho_{\mathrm{rock,mean}}$ (kg m^{-3})	1994	2352	2181
T_b (K)	272.5	272.4578	272.356
q_{surf} (mW m^{-2})	17.6	23.1	9.4
q_{con} (mW m^{-2})	24.1	27.4	15.1
η_{con} (Pa s)	2.40×10^{14}	2.37×10^{14}	2.28×10^{14}
D_{Ih} (km)	28.8	20.9	50.0
D_{ocean} (km)	59.5	37.0	48.7
$\overline{\sigma}_{\mathrm{ocean}}$ (S m^{-1})	1.0	1.0	1.0
R_{surf} (km)	198.2	252.1	235.8
R_{rock} (km)	110.0	194.3	137.0
ϕ_{rock}	0.50	0.32	0.32

Table 10. Measured and assumed properties used in default models for the moons of Jupiter. The extreme pore closure pressure and rock porosity required to find a valid Callisto model imply that it is either far from hydrostatic equilibrium or contains extraordinarily low-density rock phases in its interior. The unrealistically low surface heat flux for Io is a requirement imposed by the current lack of a convection model for rocks in *PlanetProfile*. However, matching the MoI for this body suggests that the density structure is a reasonable match, so this model provides a starting point for future work, *e.g.,* with a manually adjusted thermal profile.

Property	Io	Europa	Ganymede	Callisto
Radius R (km)[a]	1821.49	1560.8	2631.2	2410.3
Total mass M (kg)[b]	8.932×10^{22}	4.800×10^{22}	1.4819×10^{23}	1.0759×10^{23}
Axial MoI C/MR^2	0.37685 ± 0.00035 [c]	0.346 ± 0.005 [d]	0.3115 ± 0.0028 [e]	$0.3549^{+0.0042}_{-0.0148}$ [f,g]
Surface pressure P_{surf} (MPa)	0	0	0	0
Surface temperature T_{surf} (K)	110	110	110	110
Ocean composition and salinity w	N/A	35.16504 g kg^{-1} Seawater	Pure H_2O	100 g kg^{-1} $MgSO_4$
Ice bottom temperature T_b	N/A	268.305 K	258.86 K	262.0 K
Surface heat flux q_{surf}	0.14 W m^{-2}	N/A	N/A	N/A
Rock composition	CV chondrite	CM chondrite	CM chondrite	Comet 67P/C–G
Core FeS/Fe ratio	12.5 wt% FeS	20 wt% FeS	20 wt% FeS	not modeled
Ice porosity in vacuum ϕ_{ice}	N/A	not modeled	not modeled	not modeled
Ice pore closure pressure $P_{c,\mathrm{ice}}$	-	-	-	-
Rock porosity in vacuum ϕ_{rock}	70 vol%	not modeled	not modeled	90 vol%
Rock pore closure pressure $P_{c,\mathrm{rock}}$	750 MPa	-	-	4000 MPa

[a] Mean radii from Archinal et al. (2018)

[b] Hussmann et al. (2006)

[c] Anderson, Jacobson, Lau, et al. (2001)

[d] Anderson et al. (1998)

[e] Schubert et al. (2004)

[f] Anderson, Jacobson, McElrath, et al. (2001)

[g] Lower value increased by 3% of mean value per Gao and Stevenson (2013)

Table 11. Measured and assumed properties used in default models for the moons of Saturn. As with Callisto, the large reported MoI values for Titan require extreme porosity conditions to achieve valid models that match reported mass and MoI values.

Property	Mimas	Enceladus	Dione	Rhea	Titan
Radius R (km)[a]	198.2	252.1	561.4	763.5	2574.73
Total mass M (kg)[b]	3.7493×10^{19}	1.08022×10^{20}	1.095452×10^{21}	2.306518×10^{21}	1.3452×10^{23}
Axial MoI C/MR^2	0.355 ± 0.010 [c]	0.335 ± 0.001 [d]	0.33 ± 0.01 [e]	0.3721 ± 0.0036 [f]	$0.341^{+0.010}_{-0.020}$ [g,h]
Surface pressure $P_{\rm surf}$ (MPa)	0	0	0	0	0.15
Surface temperature $T_{\rm surf}$ (K)	80 [i]	75	75	75 [j]	94
Ocean composition and salinity w	$10\,{\rm g\,kg^{-1}}$ Seawater	$10\,{\rm g\,kg^{-1}}$ Seawater [k]	$10\,{\rm g\,kg^{-1}}$ Seawater	$10\,{\rm g\,kg^{-1}}$ Seawater	$100\,{\rm g\,kg^{-1}}$ $MgSO_4$
Ice bottom temperature T_b	272.5 K [l]	272.4578 K	270.93 K	265.0 K [m]	255.0 K
Surface heat flux $q_{\rm surf}$	N/A	N/A	N/A	N/A	N/A
Rock composition	Comet 67P/C–G	Comet 67P/C–G	Comet 67P/C–G	Comet 67P/C–G	Comet 67P/C–G
Core FeS/Fe ratio	not modeled	not modeled	not modeled	not modeled	not modeled
Ice porosity in vacuum $\phi_{\rm ice}$	not modeled	not modeled	not modeled	not modeled	not modeled
Ice pore closure pressure $P_{c,\rm ice}$	-	-	-	-	-
Rock porosity in vacuum $\phi_{\rm rock}$	50 vol%	32 vol%	50 vol%	92 vol%	90 vol%
Rock pore closure pressure $P_{c,\rm rock}$	350 MPa	350 MPa	350 MPa	550 MPa	2000 MPa

[a] Mean radii from Archinal et al. (2018)
[b] Jacobson et al. (2006)
[c] Hussmann et al. (2006); Tajeddine et al. (2014)
[d] Iess et al. (2014)
[e] Zannoni et al. (2020)
[f] Iess et al. (2007)
[g] Durante et al. (2019); uncertainty is not reported for this value
[h] Lower value increased by 3% of mean value per Gao and Stevenson (2013)
[i] Rhoden and Walker (2022)
[j] Howett et al. (2010)
[k] Glein et al. (2018)
[l] Tajeddine et al. (2014)
[m] Results in a completely frozen hydrosphere with $T_b = 103$ K

Table 12. Measured and assumed properties used in default models for the moons of Uranus.

Property	Miranda	Ariel	Umbriel	Titania	Oberon
Radius R (km)[a]	235.8	578.9	584.7	788.9	761.4
Total mass M (kg)[b]	0.659×10^{20}	1.353×10^{21}	1.172×10^{21}	3.527×10^{21}	3.014×10^{21}
Axial MoI C/MR^2 [c]	0.35 ± 0.03	0.306 ± 0.030	0.319 ± 0.030	0.306 ± 0.030	0.307 ± 0.030
Surface pressure $P_{\rm surf}$ (MPa)	0	0	0	0	0
Surface temperature $T_{\rm surf}$ (K)	60	60	60	60	60
Ocean composition and salinity w	$10\,{\rm g\,kg^{-1}}$ Seawater	$10\,{\rm g\,kg^{-1}}$ Seawater	$10\,{\rm g\,kg^{-1}}$ Seawater	$10\,{\rm g\,kg^{-1}}$ Seawater	$10\,{\rm g\,kg^{-1}}$ Seawater
Ice bottom temperature T_b	272.356 K	270.93 K	270.93 K	269.4 K	269.4 K
Surface heat flux $q_{\rm surf}$	N/A	N/A	N/A	N/A	N/A
Rock composition	Comet 67P/C–G	Comet 67P/C–G	CI chondrite	CI chondrite	CI chondrite
Core FeS/Fe ratio	not modeled	not modeled	not modeled	not modeled	not modeled
Ice porosity in vacuum $\phi_{\rm ice}$	not modeled	not modeled	not modeled	not modeled	not modeled
Ice pore closure pressure $P_{c,\rm ice}$	-	-	-	-	-
Rock porosity in vacuum $\phi_{\rm rock}$	32 vol%	35 vol%	10 vol%	10 vol%	10 vol%
Rock pore closure pressure $P_{\rm c,rock}$	350 MPa	450 MPa	450 MPa	450 MPa	450 MPa

[a] Mean radii from Archinal et al. (2018)

[b] Jacobson et al. (1992)

[c] Hussmann et al. (2006); large uncertainties estimated based on source methods

Table 13. Measured and assumed properties used in default models for Triton and Pluto.

Property	Triton	Pluto
Radius R (km)[a]	1352.6	1188.3
Total mass M (kg)	2.141×10^{22} [b]	1.303×10^{22} [c]
Axial MoI C/MR^2	0.31 ± 0.03 [d]	0.31 ± 0.03
Surface pressure P_{surf} (MPa)	0	0
Surface temperature T_{surf} (K)	38	44
Ocean composition and salinity w	$10\,\mathrm{g\,kg^{-1}}$ $MgSO_4$	$50\,\mathrm{g\,kg^{-1}}$ $MgSO_4$
Ice bottom temperature T_b	266.0 K	265.0 K
Surface heat flux q_{surf}	N/A	N/A
Rock composition	Comet 67P/C–G	Comet 67P/C–G
Core FeS/Fe ratio	not modeled	not modeled
Ice porosity in vacuum ϕ_{ice}	not modeled	not modeled
Ice pore closure pressure $P_{c,\mathrm{ice}}$	-	-
Rock porosity in vacuum ϕ_{rock}	35 vol%	35 vol%
Rock pore closure pressure $P_{c,\mathrm{rock}}$	350 MPa	350 MPa

[a] Mean radii from Archinal et al. (2018)

[b] Tyler et al. (1989)

[c] Brozović et al. (2015)

[d] Hussmann et al. (2006); large uncertainties estimated based on source methods

Future investigations of icy bodies will rely heavily on gravitational fields, magnetic fields, and remote sensing to constrain their interior structures. *PlanetProfile* is the only open-source software yet available that self-consistently relates bulk properties of icy bodies derived from spacecraft gravity measurements—through an ocean EOS including electrical conductivity—to the induced magnetic fields expected from their subsurface oceans. Integration with other open-source software packages is essential to this key feature. Incorporating measurements from as many sources as possible to better constrain the results is vital, and represents a major motivation for the design of *PlanetProfile*.

Because *PlanetProfile* models rely on laboratory measurements to inform the ocean and pore fluid EOS, the models are limited to those compositions for which such measurements exist or can be reliably extrapolated into the regions of interest. Due to the lack of suitable measurements in many pure (binary) and all mixed aqueous systems, the modeled oceans are restricted to a handful of end-member cases for their solutes, and for larger bodies, only a single dissolved solute type can be studied.

Clathrates of volatile species (*e.g.,* CH_4 and CO_2) and ions are likely common in the outer solar system (Hand et al., 2006; Journaux et al., 2013; Mousis et al., 2015). Measurements of clathrates at relevant conditions are also lacking, especially for mixtures of guest molecules and amalgamated layers of ice and clathrates. Laboratory measurements of the relevant properties of these materials can dramatically affect models that incorporate them, especially when the alternative is to omit materials with insufficient data.

PlanetProfile currently does not model convection in rock layers. Not including this process restricts the applicability of fully self-consistent models to those that do not reach internal temperatures warm enough to convect. Such assumptions have typically been regarded as valid because of the prevailing view that tidally generated heat concentrates in the icy lithosphere (Tobie et al., 2005; Kang & Flierl, 2020). This view has been challenged by inferences of hydrothermal minerals in the Enceladus E-ring (Hsu et al., 2015) and recent 3D models of Europa's tides (Běhounková et al., 2021), opening a larger parameter space of models to explore in future work. In these cases, the current release of *PlanetProfile* remains useful for exploring planetary properties, especially for bodies with substantial overlying oceans.

Convection is important for bodies like Io with a high surface heat flux, although here as well convection may be limited in favor of heat transport through melt migration (Moore, 2003). The mass- and MoI-matching density profile evaluated with *PlanetProfile* for non-convecting bodies offers a valuable starting point for further modeling to improve self-consistency. Implementing self-consistent convection in rocks is a top priority for future development. In addition, modeling of partial melts will allow investigation of unresolved questions at Io, including whether a magma ocean may be present there (Khurana et al., 2011) despite the challenges this presents to meet the relatively high mantle viscosity (of order $10^{16}\,\mathrm{Pa\,s}$) needed to sustain the observed surface heat flux of $2.24\,\mathrm{W\,m^{-2}}$ (Lainey et al., 2009).

For partially differentiated bodies like Callisto, Rhea, and Titan, mixed ice/fluid/rock interior layers are modeled using an effective porosity. Deep inside Callisto and Titan, the great overburden pressure should tend to close pores, consistent with models for thermally induced and tectonic fracturing (Vance et al., 2007; Klimczak et al., 2019). The porosity model we employ (Han et al., 2014) requires very large pore closure pressures and vacuum-equivalent porosities in order to generate valid profiles that match the high MoIs. This result has a few possible implications: 1) The rock matrix includes very low-density silicates or large amounts of high-pressure ices or both. A mixed ice–rock "snowball" has been suggested as an explanation for Callisto (Schubert et al., 2004), which fits with this interpretation. 2) The bodies are very homogeneous in their interiors. Such homogeneity requires low-density mineralogies. The carbonaceous silicate interior model for Titan suggested by Néri et al. (2020) offers one such scenario. 3) The Han et al. (2014) exponential model is not valid for the mixed material phases that we assume. Alternative porosity models must still account for the migration and fate of volatiles and ices in the rocky interiors of large ocean worlds. Related studies of Europa's early metamorphic outgassing in relation to the formation of its ocean retain extensive volatiles in the rocky interior without quantifying the implied porosities involved (Melwani Daswani et al., 2021).

Converting the ocean melting temperature input to a surface heat flux input for ice shells, and self-consistently calculating convection from these, is another top priority for future development. Valid models for Rhea suggest it has a completely frozen hydrosphere, but the temperature at the ice–rock interface cannot be determined self-consistently in *PlanetProfile* because the ocean melting temperature is a model input. This present

limitation adds uncertainty to the rock densities determined from the EOS for Rhea, and hence the mass- and MoI-matching are biased to structural solutions that include oceans.

PlanetProfile is a versatile tool that can be applied to study a wide array of problems in understanding planetary bodies in the solar system and beyond. The software is open-source and frequently updated. As more laboratory measurements become available, it will be possible to use *PlanetProfile* to explore an ever-greater space of possible configurations.

Open Research

Data used in this work were generated using the open-source *PlanetProfile* software hosted on GitHub. A Zenodo archive of the most recent version is available at `https://doi.org/10.5281/zenodo.844130` (Styczinski, Vance, Niesyt, et al., 2022). *PlanetProfile* is released under a GNU GPL-v3.0 license. The v2.3.3 release associated with this manuscript is archived at `https://doi.org/10.5281/zenodo.7319838` (Styczinski, Vance, Niesyt, et al., 2022). A Zenodo archive of the output data for default models is available at `https://doi.org/10.5281/zenodo.7250785` (Styczinski, Vance, & Daswani, 2022a). A Zenodo archive of models generated for comparison to Vance et al. (2018) is available at `https://doi.org/10.5281/zenodo.7318029` (Styczinski, Vance, & Daswani, 2022b). The v1.0.0 release associated with Vance et al. (2018) is archived at `https://doi.org/10.5281/zenodo.844131` (Vance, 2017).

Acknowledgments

M.J.S. thanks S. Stähler for direction on creating files compatible with *AxiSEM*, A. Bryant and M. Panning for the same with *Mineos*, and E. Leonard and S. Eilenberg for helpful discussions. This work was carried out at the Jet Propulsion Laboratory, California Institute of Technology, under a contract with NASA (80NM0018D0004). The authors acknowledge that portions of this work have been carried out on the traditional lands of the Tongva people. M.J.S. was supported by an appointment to the NASA Postdoctoral Program at the Jet Propulsion Laboratory, California Institute of Technology, administered by Oak Ridge Associated Universities under a contract with NASA (80HQTR21CA005). M.M.D. was supported by NASA grant NNH18ZDA001N-HW:Habitable Worlds and NASA Planetary Science Early Career Award NNH19ZDA001N-ECA.

References

Anderson, J. D., Jacobson, R. A., Lau, E. L., Moore, W. B., & Schubert, G. (2001). Io's gravity field and interior structure. *Journal of Geophysical Research: Planets*, *106*(E12), 32963–32969.

Anderson, J. D., Jacobson, R. A., McElrath, T. P., Moore, W. B., Schubert, G., & Thomas, P. C. (2001). Shape, mean radius, gravity field, and interior structure of Callisto. *Icarus*, *153*(1), 157–161.

Anderson, J. D., Lau, E. L., Sjogren, W. L., Schubert, G., & Moore, W. B. (1996). Gravitational constraints on the internal structure of Ganymede. *Nature*, *384*(6609), 541–543.

Anderson, J. D., Schubert, G., Jacobson, R. A., Lau, E. L., Moore, W. B., & Sjogren, W. L. (1998). Europa's differentiated internal structure: Inferences from four Galileo encounters. *Science*, *281*(5385), 2019–2022. doi: 10.1126/science.281.5385.2019

Andersson, O., & Inaba, A. (2005). Thermal conductivity of crystalline and amorphous ices and its implications on amorphization and glassy water. *Physical Chemistry Chemical Physics*, *7*(7), 1441–1449.

Archinal, B. A., Acton, C. H., A'Hearn, M. F., Conrad, A., Consolmagno, G. J., Duxbury, T., ... Williams, I. P. (2018). Report of the IAU working group on cartographic coordinates and rotational elements: 2015. *Celestial Mechanics and Dynamical Astronomy*, *130*(3), 22. doi: 10.1007/s10569-017-9805-5

Bardyn, A., Baklouti, D., Cottin, H., Fray, N., Briois, C., Paquette, J., ... Hilchenbach, M. (2017). Carbon-rich dust in comet 67P/Churyumov-Gerasimenko measured by COSIMA/Rosetta. *Monthly Notices of the Royal Astronomical Society*, *469*(Suppl_2), S712–S722.

Běhounková, M., Tobie, G., Choblet, G., Kervazo, M., Daswani, M. M., Dumoulin, C., & Vance, S. D. (2021). Tidally induced magmatic pulses on the oceanic floor of Jupiter's moon Europa. *Geophysical Research Letters*, *48*(3). Retrieved from `https://doi.org/10.1029\%2F2020gl090077` doi: 10.1029/2020gl090077

Beuthe, M., Rivoldini, A., & Trinh, A. (2016). Enceladus's and Dione's floating ice shells supported by minimum stress isostasy. *Geophysical Research Letters*, *43*(19), 10–088.

Beyreuther, M., Barsch, R., Krischer, L., Megies, T., Behr, Y., & Wassermann, J. (2010). ObsPy: A Python toolbox for seismology. *Seismological Research Letters*, *81*(3), 530–533.

Bollengier, O., Brown, J. M., & Shaw, G. H. (2019). Thermodynamics of pure liquid water: Sound speed measurements to 700 MPa down to the freezing point, and an equation of state to 2300 MPa from 240 to 500 K. *The Journal of Chemical Physics*, *151*(5), 054501.

Brozović, M., Showalter, M. R., Jacobson, R. A., & Buie, M. W. (2015). The orbits and masses of satellites of Pluto. *Icarus*, *246*, 317–329.

Chatterjee, N. D., & Froese, E. (1975). A thermodynamic study of the pseudobinary join muscovite-paragonite in the system $KAlSi_3O_8$-$NaAlSi_3O_8$-Al_2O_3-SiO_2-H_2O. *American Mineralogist*, *60*(11-12), 985–993.

Choukroun, M., & Grasset, O. (2010). Thermodynamic data and modeling of the water and ammonia–water phase diagrams up to 2.2 GPa for planetary geophysics. *The Journal of chemical physics*, *133*(14), 144502.

Choukroun, M., Grasset, O., Tobie, G., & Sotin, C. (2010). Stability of methane clathrate hydrates under pressure: Influence on outgassing processes of methane on Titan. *Icarus*, *205*(2), 581–593.

Cockell, C. S., Bush, T., Bryce, C., Direito, S., Fox-Powell, M., Harrison, J. P., ... Zorzano, M. P. (2016). Habitability: A Review. *Astrobiology*, *16*(1), 89–117. doi: 10.1089/ast.2015.1295

Connolly, J. A. D. (2009). The geodynamic equation of state: what and how. *Geochemistry, geophysics, geosystems*, *10*(10).

Connolly, J. A. D., & Galvez, M. E. (2018). Electrolytic fluid speciation by Gibbs energy minimization and implications for subduction zone mass transfer. *Earth and Planetary Science Letters*, *501*, 90–102. doi: 10.1016/j.epsl.2018.08.024

Cottaar, S., Heister, T., Rose, I., & Unterborn, C. (2014). BurnMan: A lower mantle mineral physics toolkit. *Geochemistry, Geophysics, Geosystems*, *15*(4), 1164–1179.

Crotwell, H. P., Owens, T. J., & Ritsema, J. (1999). The TauP Toolkit: Flexible seismic travel-time and ray-path utilities. *Seismological Research Letters*, *70*, 154–160. doi: 10.1785/gssrl.70.2.154

Deschamps, F., & Sotin, C. (2001). Thermal convection in the outer shell of large

icy satellites. *Journal of Geophysical Research: Planets*, *106*(E3), 5107–5121.

Dhooghe, F., De Keyser, J., Altwegg, K., Briois, C., Balsiger, H., Berthelier, J.-J., ... Wurz, P. (2017). Halogens as tracers of protosolar nebula material in comet 67P/Churyumov–Gerasimenko. *Monthly Notices of the Royal Astronomical Society*, *472*(2), 1336–1345.

Durante, D., Hemingway, D. J., Racioppa, P., Iess, L., & Stevenson, D. J. (2019). Titan's gravity field and interior structure after Cassini. *Icarus*, *326*, 123–132.

Dziewonski, A. M., & Anderson, D. L. (1981). Preliminary reference Earth model. *Physics of the earth and planetary interiors*, *25*(4), 297–356.

Feistel, R., & Wagner, W. (2006). A new equation of state for h_2o ice Ih. *Journal of Physical and Chemical Reference Data*, *35*(2), 1021–1047.

Filacchione, G., Groussin, O., Herny, C., Kappel, D., Mottola, S., Oklay, N., ... Raponi, A. (2019). Comet 67P/CG nucleus composition and comparison to other comets. *Space science reviews*, *215*(1), 1–46.

Gao, P., & Stevenson, D. J. (2013). Nonhydrostatic effects and the determination of icy satellites' moment of inertia. *Icarus*, *226*(2), 1185–1191.

Glein, C. R., Postberg, F., & Vance, S. D. (2018). The geochemistry of Enceladus: composition and controls. In P. M. Schenk, R. N. Clark, C. J. A. Howett, A. J. Verbiscer, & J. H. Waite (Eds.), *Enceladus and the icy moons of Saturn* (pp. 39–56). Tucson: University of Arizona Press.

Glein, C. R., & Waite, J. H. (2020). The carbonate geochemistry of Enceladus' ocean. *Geophysical Research Letters*, *47*(3), e2019GL085885.

Glover, P. W. J., & Vine, F. J. (1994). Electrical conductivity of the continental crust. *Geophysical research letters*, *21*(22), 2357–2360.

Green, E., Holland, T. J. B., & Powell, R. (2007). An order-disorder model for omphacitic pyroxenes in the system jadeite-diopside-hedenbergite-acmite, with applications to eclogitic rocks. *American Mineralogist*, *92*(7), 1181–1189. doi: 10.2138/am.2007.2401

Hammond, N. P., Barr, A. C., & Parmentier, E. M. (2016). Recent tectonic activity on Pluto driven by phase changes in the ice shell. *Geophysical Research Letters*, *43*(13), 6775–6782.

Han, S.-C., Schmerr, N., Neumann, G., & Holmes, S. (2014). Global characteristics of porosity and density stratification within the lunar crust from GRAIL grav-

ity and Lunar Orbiter Laser Altimeter topography data. *Geophysical Research Letters*, *41*(6), 1882–1889.

Hand, K., Chyba, C., Carlson, R., & Cooper, J. (2006). Clathrate Hydrates of Oxidants in the Ice Shell of Europa. *Astrobiology*, *6*(3), 463–482.

Helgerud, M., Waite, W. F., Kirby, S., & Nur, A. (2009). Elastic wave speeds and moduli in polycrystalline ice Ih, sI methane hydrate, and sII methane-ethane hydrate. *Journal of Geophysical Research: Solid Earth*, *114*(B2).

Hemingway, D. J., & Mittal, T. (2019). Enceladus's ice shell structure as a window on internal heat production. *Icarus*, *332*, 111–131.

Holland, T. J. B., Baker, J., & Powell, R. (1998). Mixing properties and activity-composition relationships of chlorites in the system MgO-FeO-Al_2O_3-SiO_2-H_2O. *European Journal of Mineralogy*, *10*(3), 395–406. doi: 10.1127/ejm/10/3/0395

Holland, T. J. B., Green, E. C. R., & Powell, R. (2018). Melting of peridotites through to granites: A simple thermodynamic model in the system KNCF-MASHTOCr. *Journal of Petrology*, *59*(5), 881–900. doi: 10.1093/petrology/egy048

Holland, T. J. B., & Powell, R. (1998). An internally consistent thermodynamic data set for phases of petrological interest. *Journal of metamorphic Geology*, *16*(3), 309–343.

Holland, T. J. B., & Powell, R. (2011). An improved and extended internally consistent thermodynamic dataset for phases of petrological interest, involving a new equation of state for solids. *Journal of Metamorphic Geology*, *29*, 333.

Howett, C. J. A., Spencer, J. R., Pearl, J., & Segura, M. (2010). Thermal inertia and bolometric Bond albedo values for Mimas, Enceladus, Tethys, Dione, Rhea and Iapetus as derived from Cassini/CIRS measurements. *Icarus*, *206*(2), 573–593.

Hsu, H.-W., Postberg, F., Sekine, Y., Shibuya, T., Kempf, S., Horányi, M., ... Srama, R. (2015). Ongoing hydrothermal activities within Enceladus. *Nature*, *519*(7542), 207–210.

Hussmann, H., Sohl, F., & Spohn, T. (2006). Subsurface oceans and deep interiors of medium-sized outer planet satellites and large trans-neptunian objects. *Icarus*, *185*(1), 258–273.

Iess, L., Rappaport, N. J., Tortora, P., Lunine, J., Armstrong, J. W., Asmar, S. W., ... Zingoni, F. (2007). Gravity field and interior of Rhea from Cassini data analysis. *Icarus*, *190*(2), 585–593.

Iess, L., Stevenson, D., Parisi, M., Hemingway, D., Jacobson, R., Lunine, J., ... Tortora, P. (2014). The gravity field and interior structure of Enceladus. *Science*, *344*(6179), 78–80.

Jacobson, R. A., Antreasian, P. G., Bordi, J. J., Criddle, K. E., Ionasescu, R., Jones, J. B., ... Stauch, J. R. (2006). The gravity field of the saturnian system from satellite observations and spacecraft tracking data. *The Astronomical Journal*, *132*(6), 2520.

Jacobson, R. A., Campbell, J. K., Taylor, A. H., & Synnott, S. P. (1992). The masses of Uranus and its major satellites from Voyager tracking data and Earth-based Uranian satellite data. *The Astronomical Journal*, *103*, 2068–2078.

Jennings, E. S., Holland, T. J. B., Shorttle, O., Maclennan, J., & Gibson, S. A. (2016). The composition of melts from a heterogeneous mantle and the origin of ferropicrite: Application of a thermodynamic model. *Journal of Petrology*, *57*, 2289–2310. doi: 10.1093/petrology/egw065

Journaux, B., Brown, J. M., Pakhomova, A., Collings, I. E., Petitgirard, S., Espinoza, P., ... Hanfland, M. (2020). Holistic approach for studying planetary hydrospheres: Gibbs representation of ices thermodynamics, elasticity, and the water phase diagram to 2,300 MPa. *Journal of Geophysical Research: Planets*, *125*(1), e2019JE006176.

Journaux, B., Daniel, I., Caracas, R., Montagnac, G., & Cardon, H. (2013). Influence of NaCl on ice VI and ice VII melting curves up to 6 GPa, implications for large icy moons. *Icarus*, *226*(1), 355–363.

Kamata, S., Nimmo, F., Sekine, Y., Kuramoto, K., Noguchi, N., Kimura, J., & Tani, A. (2019). Pluto's ocean is capped and insulated by gas hydrates. *Nature Geoscience*, *12*(6), 407–410.

Kang, W., & Flierl, G. (2020). Spontaneous formation of geysers at only one pole on Enceladus's ice shell. *Proceedings of the National Academy of Sciences*, *117*(26), 14764–14768.

Khurana, K. K., Jia, X., Kivelson, M. G., Nimmo, F., Schubert, G., & Russell, C. T.

(2011). Evidence of a global magma ocean in Io's interior. *Science*, *332*(6034), 1186–1189.

Khurana, K. K., Kivelson, M. G., & Russell, C. T. (2002). Searching for liquid water in Europa by using surface observatories. *Astrobiology*, *2*(1), 93–103. doi: 10.1089/153110702753621376

Kimura, J., & Kamata, S. (2020). Stability of the subsurface ocean of Pluto. *Planetary and Space Science*, *181*, 104828.

Kivelson, M. G., Khurana, K. K., Russell, C. T., Volwerk, M., Walker, R. J., & Zimmer, C. (2000). Galileo magnetometer measurements: A stronger case for a subsurface ocean at Europa. *Science*, *289*(5483), 1340–1343. doi: 10.1126/science.289.5483.1340

Klimczak, C., Byrne, P. K., Regensburger, P. V., Bohnenstiehl, D. R., Hauck, S. A., Dombard, A. J., ... Elder, C. M. (2019). Strong ocean floors within Europa, Titan, and Ganymede limit geological activity there; Enceladus less so. In *50th annual lunar and planetary science conference* (p. 2912).

Lainey, V., Arlot, J.-E., Karatekin, Ö., & Van Hoolst, T. (2009). Strong tidal dissipation in Io and Jupiter from astrometric observations. *Nature*, *459*(7249), 957–959.

Larionov, E., & Kryukov, P. (1984). The conductivity of $MgSO_4$ aqueous-solutions in the range of temperatures 298–423 K and pressures 0.1–784.6 MPa. *Izvestiya Sibirskogo Otdeleniya Akademii Nauk SSSR Seriya Khimicheskikh Nauk*, *5*, 20–23.

Le Roy, L., Altwegg, K., Balsiger, H., Berthelier, J.-J., Bieler, A., Briois, C., ... Tzou, C.-y. (2015). Inventory of the volatiles on comet 67P/Churyumov-Gerasimenko from Rosetta/ROSINA. *Astronomy & Astrophysics*, *583*, A1.

Light, T. S., Licht, S., Bevilacqua, A. C., & Morash, K. R. (2004). The fundamental conductivity and resistivity of water. *Electrochemical and solid-state letters*, *8*(1), E16.

Lodders, K. (2021). Relative atomic solar system abundances, mass fractions, and atomic masses of the elements and their isotopes, composition of the solar photosphere, and compositions of the major chondritic meteorite groups. *Space Science Reviews*, *217*(3), 44. doi: 10.1007/s11214-021-00825-8

Lodders, K., & Fegley, B. (1998). *The planetary scientist's companion.* Oxford Uni-

versity Press on Demand.

McDougall, T. J., & Barker, P. M. (2011). Getting started with TEOS-10 and the Gibbs seawater (GSW) oceanographic toolbox. *SCOR/IAPSO WG*, *127*, 1–28.

McKinnon, W. B. (2006). On convection in ice I shells of outer solar system bodies, with detailed application to Callisto. *Icarus*, *183*(2), 435–450.

Melini, D., Saliby, C., & Spada, G. (2022). On computing viscoelastic Love numbers for general planetary models: the ALMA3 code. *Geophysical Journal International*, *231*(3), 1502–1517.

Melosh, H. J., Ekholm, A. G., Showman, A. P., & Lorenz, R. D. (2004). The temperature of Europa's subsurface water ocean. *Icarus*, *168*(2), 498–502.

Melwani Daswani, M., Vance, S. D., Mayne, M. J., & Glein, C. R. (2021). A metamorphic origin for Europa's ocean. *Geophysical Research Letters*. (under revision)

Moore, W. B. (2003). Tidal heating and convection in Io. *Journal of Geophysical Research: Planets*, *108*(E8), 5096.

Morin, D. (2008). *Introduction to classical mechanics: with problems and solutions*. Cambridge University Press.

Mousis, O., Chassefière, E., Holm, N. G., Bouquet, A., Waite, J. H., Geppert, W. D., ... Rousselot, P. (2015). Methane clathrates in the solar system. *Astrobiology*, *15*(4), 308-326. doi: 10.1089/ast.2014.1189

Néri, A., Guyot, F., Reynard, B., & Sotin, C. (2020). A carbonaceous chondrite and cometary origin for icy moons of Jupiter and Saturn. *Earth and Planetary Science Letters*, *530*, 115920.

Nimmo, F., Hamilton, D. P., McKinnon, W. B., Schenk, P. M., Binzel, R. P., Bierson, C. J., ... The New Horizons Geology, Geophysics & Imaging Theme Team (2016). Reorientation of Sputnik Planitia implies a subsurface ocean on Pluto. *Nature*, *540*(7631), 94–96.

Nimmo, F., & Pappalardo, R. T. (2016). Ocean worlds in the outer solar system. *Journal of Geophysical Research: Planets*, *121*(8), 1378–1399.

Ning, F., Glavatskiy, K., Ji, Z., Kjelstrup, S., & Vlugt, T. H. (2015). Compressibility, thermal expansion coefficient and heat capacity of ch_4 and co_2 hydrate mixtures using molecular dynamics simulations. *Physical Chemistry Chemical*

Physics, *17*(4), 2869–2883.

Nissen-Meyer, T., van Driel, M., Stähler, S. C., Hosseini, K., Hempel, S., Auer, L., ... Fournier, A. (2014). AxiSEM: broadband 3-D seismic wavefields in axisymmetric media. *Solid Earth*, *5*(1), 425–445.

Padrón-Navarta, J. A., Sánchez-Vizcaíno, V. L., Hermann, J., Connolly, J. A., Garrido, C. J., Gómez-Pugnaire, M. T., & Marchesi, C. (2013). Tschermak's substitution in antigorite and consequences for phase relations and water liberation in high-grade serpentinites. *Serpentinites from mid-oceanic ridges to subduction*, *178*, 186–196. doi: 10.1016/j.lithos.2013.02.001

Pätzold, M., Andert, T., Hahn, M., Asmar, S. W., Barriot, J.-P., Bird, M. K., ... Scholten, F. (2016). A homogeneous nucleus for comet 67P/Churyumov–Gerasimenko from its gravity field. *Nature*, *530*(7588), 63–65.

Petrenko, V. F., & Schulson, E. M. (1992). The effect of static electric fields on protonic conductivity of ice single crystals. *Philosophical Magazine B*, *66*(3), 341–353.

Pozzo, M., Davies, C., Gubbins, D., & Alfè, D. (2012). Thermal and electrical conductivity of iron at Earth's core conditions. *Nature*, *485*(7398), 355–358.

Quist, A. S., & Marshall, W. L. (1968). Electrical conductances of aqueous sodium chloride solutions from 0 to 800° and at pressures to 4000 bars. *The journal of physical chemistry*, *72*(2), 684–703.

Rambaux, N., & Castillo-Rogez, J. (2013). Tides on satellites of giant planets. In J. Souchay, S. Mathis, & T. Tokieda (Eds.), *Tides in astronomy and astrophysics* (pp. 167–200). Springer-Verlag Berlin Heidelberg. doi: 10.1007/978-3-642-32961-6_5

Rhoden, A. R., & Walker, M. E. (2022). The case for an ocean-bearing Mimas from tidal heating analysis. *Icarus*, *376*, 114872.

Rothschild, L. J., & Mancinelli, R. L. (2001). Life in extreme environments. *Nature*, *409*(6823), 1092–1101.

Saxena, S., & Eriksson, G. (2015). Thermodynamics of Fe–S at ultra-high pressure. *Calphad*, *51*, 202–205. doi: 10.1016/j.calphad.2015.09.009

Schubert, G., Anderson, J. D., Spohn, T., & McKinnon, W. B. (2004). Interior composition, structure and dynamics of the Galilean satellites. In F. Bagenal, T. Dowling, & W. McKinnon (Eds.), *Jupiter: The planet, satellites and*

magnetosphere (pp. 281–306). Cambridge University Press.

Sloan, E. (1998). Physical/chemical properties of gas hydrates and application to world margin stability and climatic change. *Geological society, London, special publications*, *137*(1), 31–50.

Solomatov, V. S. (1995). Scaling of temperature-and stress-dependent viscosity convection. *Physics of Fluids*, *7*(2), 266–274.

Spada, G. (2008). ALMA, a Fortran program for computing the viscoelastic Love numbers of a spherically symmetric planet. *Computers & Geosciences*, *34*(6), 667–687.

Stähler, S. C., Panning, M. P., Vance, S. D., Lorenz, R. D., van Driel, M., Nissen-Meyer, T., & Kedar, S. (2018). Seismic wave propagation in icy ocean worlds. *Journal of Geophysical Research: Planets*, *123*(1), 206–232.

Staley, D. O. (1970). The adiabatic lapse rate in the Venus atmosphere. *Journal of the Atmospheric Sciences*, *27*(2), 219–223.

Stern, L. A., Constable, S., Lu, R., Du Frane, W. L., & Roberts, J. J. (2021). Electrical properties of carbon dioxide hydrate: Implications for monitoring CO_2 in the gas hydrate stability zone. *Geophysical Research Letters*, *48*(15), e2021GL093475.

Styczinski, M. J., Vance, S. D., & Daswani, M. M. (2022a). *Planetprofile default model outputs* [Dataset]. Zenodo. Retrieved from `https://doi.org/10.5281/zenodo.7319854` doi: 10.5281/zenodo.7319854

Styczinski, M. J., Vance, S. D., & Daswani, M. M. (2022b). *PlanetProfile Python version outputs compared to models of Vance et al. (2018)* [Dataset]. Zenodo. Retrieved from `https://doi.org/10.5281/zenodo.7318030` doi: 10.5281/zenodo.7318030

Styczinski, M. J., Vance, S. D., Harnett, E. M., & Cochrane, C. J. (2022). A perturbation method for evaluating the magnetic field induced from an arbitrary, asymmetric ocean world analytically. *Icarus*, *376*(1), 114840. Retrieved from `https://doi.org/10.1016/j.icarus.2021.114840`

Styczinski, M. J., Vance, S. D., Niesyt, M., Lisitsyn, A., Daswani, M. M., Marusiak, A. G., ... Bryant, A. S. (2022). *vancesteven/PlanetProfile: Fix mantle compositions packaged in release* [Software]. Zenodo. Retrieved from `https://doi.org/10.5281/zenodo.7319838` doi: 10.5281/zenodo.7319838

Tajeddine, R., Rambaux, N., Lainey, V., Charnoz, S., Richard, A., Rivoldini, A., & Noyelles, B. (2014). Constraints on Mimas' interior from Cassini ISS libration measurements. *Science*, *346*(6207), 322–324.

Thomas, P., Tajeddine, R., Tiscareno, M., Burns, J., Joseph, J., Loredo, T., ... Porco, C. (2016). Enceladus's measured physical libration requires a global subsurface ocean. *Icarus*, *264*, 37–47.

Tobie, G., Mocquet, A., & Sotin, C. (2005). Tidal dissipation within large icy satellites: Applications to Europa and Titan. *Icarus*, *177*(2), 534–549.

Trumbo, S. K., Brown, M. E., & Hand, K. P. (2019). Sodium chloride on the surface of Europa. *Science advances*, *5*(6), eaaw7123. doi: 10.1126/sciadv.aaw7123

Turcotte, D. L., & Schubert, G. (2002). *Geodynamics*. Cambridge University Press.

Tyler, G. L., Sweetnam, D. N., Anderson, J. D., Borutzki, S. E., Campbell, J. K., Eshleman, V. R., ... Wood, G. E. (1989). Voyager radio science observations of Neptune and Triton. *Science*, *246*(4936), 1466–1473.

Vance, S. D. (2017). *vancesteven/PlanetProfile: Release for use in reproducing results submitted to Journal of Geophysical Research - Planets* [Software]. Zenodo. Retrieved from `https://doi.org/10.5281/zenodo.844131` doi: 10.5281/zenodo.844131

Vance, S. D., Bouffard, M., Choukroun, M., & Sotin, C. (2014). Ganymede's internal structure including thermodynamics of magnesium sulfate oceans in contact with ice. *Planetary and Space Science*, *96*, 62–70.

Vance, S. D., & Brown, J. M. (2013). Thermodynamic properties of aqueous $MgSO_4$ to 800 MPa at temperatures from −20 to 100°C and concentrations to 2.5 mol kg^{-1} from sound speeds, with applications to icy world oceans. *Geochimica et Cosmochimica Acta*, *110*, 176–189.

Vance, S. D., Hand, K. P., & Pappalardo, R. T. (2016). Geophysical controls of chemical disequilibria in Europa. *Geophysical Research Letters*, *43*(10), 4871–4879.

Vance, S. D., Harnmeijer, J., Kimura, J., Hussmann, H., deMartin, B., & Brown, J. M. (2007). Hydrothermal systems in small ocean planets. *Astrobiology*, *7*(6), 987-1005.

Vance, S. D., Panning, M. P., Stähler, S., Cammarano, F., Bills, B. G., Tobie, G., ... Banerdt, B. (2018). Geophysical investigations of habitability in ice-covered

ocean worlds. *Journal of Geophysical Research: Planets*, *123*(1), 180–205. doi: 10.1002/2017JE005341

Vance, S. D., Styczinski, M. J., Bills, B. G., Cochrane, C. J., Soderlund, K. M., Gómez-Pérez, N., & Paty, C. (2021). Magnetic induction responses of Jupiter's ocean moons including effects from adiabatic convection. *Journal of Geophysical Research: Planets*, *126*(2), e2020JE006418. doi: 10.1029/2020JE006418

Vitovtova, V. M., Shmonov, V. M., & Zharikov, A. V. (2014). The porosity trend and pore sizes of the rocks in the continental crust of the earth: Evidence from experimental data on permeability. *Izvestiya, Physics of the Solid Earth*, *50*(5), 593–602.

Westall, F., & Brack, A. (2018). The importance of water for life. *Space Science Reviews*, *214*(2), 1–23.

Yu, C., Ji, S., & Li, Q. (2016). Effects of porosity on seismic velocities, elastic moduli and Poisson's ratios of solid materials and rocks. *Journal of Rock Mechanics and Geotechnical Engineering*, *8*(1), 35–49.

Zannoni, M., Hemingway, D., Gomez Casajus, L., & Tortora, P. (2020). The gravity field and interior structure of Dione. *Icarus*, *345*, 113713.

Zimmer, C., Khurana, K. K., & Kivelson, M. G. (2000). Subsurface oceans on Europa and Callisto: Constraints from Galileo magnetometer observations. *Icarus*, *147*(2), 329–347. doi: 10.1006/icar.2000.6456

Zolotov, M. Y., & Kargel, J. S. (2009). On the chemical composition of Europa's icy shell, ocean, and underlying rocks. In R. T. Pappalardo, W. B. McKinnon, & K. Khurana (Eds.), *Europa* (pp. 431–456). Tucson: University of Arizona Press.